

# Leveraging TROPOMI observations and WRF-GHG modeling towards improving methane emission assessments in India

Thara Anna Mathew<sup>1,2</sup>, Dhanyalekshmi Pillai<sup>1,2</sup>, Jithin Sukumaran<sup>1,2</sup>, Monish Vijay Deshpande<sup>1,2,3</sup>, Michael Buchwitz<sup>4</sup>, Oliver Schneising<sup>4</sup>, Vishnu Thilakan<sup>1,2,5</sup>, Aparna Ravi<sup>1,2</sup>, Sanjid Backer Kanakkassery<sup>1,2,6</sup>, Sivarajan Sijikumar<sup>7</sup>, Imran A Girach<sup>8</sup>, and S Suresh Babu<sup>7</sup>

<sup>1</sup>Indian Institute of Science Education and Research Bhopal (IISERB), India

<sup>2</sup>Max Planck Partner Group (IISERB), Max Planck Society, Munich, Germany

<sup>3</sup>Now at the University of Michigan, Ann Harbor, Michigan, USA

<sup>4</sup>Institute of Environmental Physics (IUP), University of Bremen FB1, Bremen, Germany

<sup>5</sup>Now at Lund University, Lund, Sweden

<sup>6</sup>Now at Max Planck Institute for Biogeochemistry (MPI-BGC), Jena, Germany

<sup>7</sup>Space Physics Laboratory (SPL), Vikram Sarabhai Space Centre, Thiruvananthapuram, India

<sup>8</sup>Space Applications Centre (SAC), Indian Space Research Organization, Ahmedabad, India

**Correspondence:** Dhanyalekshmi Pillai (dhanya@iiserb.ac.in)

## Abstract.

Atmospheric methane (CH<sub>4</sub>) contributes to global warming and climate change. Multiple factors control its atmospheric growth rate, posing challenges for climate change mitigation in regions with limited observations, like India. In this study, we examine the potential of dry air column methane mixing ratio (XCH<sub>4</sub>) observations from the Tropospheric Monitoring Instrument (TROPOMI) in conjunction with the high-resolution Weather Research and Forecasting model with Greenhouse Gas module (WRF-GHG) to improve the annual CH<sub>4</sub> budget of India. In addition to an inversion framework, we present a spatiotemporal assessment of bottom-up Indian methane emissions and their influence on XCH<sub>4</sub>, supplying the context needed for regional emission optimization. Our analysis demonstrates the potential of WRF-GHG to represent the atmospheric XCH<sub>4</sub> and CH<sub>4</sub> distributions, including seasonal patterns, albeit with non-negligible uncertainties when compared with satellite and ground-based observations for 2018 and 2019. We find that the WRF-GHG simulations tend to overestimate XCH<sub>4</sub> while underestimating near-surface CH<sub>4</sub> concentrations at the Thumba site. Our inversion analyses report annual CH<sub>4</sub> emissions ranging from 23.3 to 25.2 Tg with an uncertainty of 3.3 Tg (anthropogenic sources), implying an overestimation of 14 to 20 % by the EDGAR global inventory. Also, our estimates are approximately 19 % higher than those in the India Fourth Biennial Update Report (19.6 Tg) and close to the latest Global Methane Budget 2000-2020. Overall, this study demonstrates the usefulness of TROPOMI observations for assessing Indian CH<sub>4</sub> emissions and shows a way to improve our understanding of how regional processes can modulate atmospheric CH<sub>4</sub> mixing ratios. We highlight the need for expanded observational coverage and an improved carbon assimilation system over India to refine the methane budget in support of global climate goals.

## 1 Introduction

20 The concentration of atmospheric CO<sub>2</sub> has increased by more than 50 % of the pre-industrial levels, while that of CH<sub>4</sub> has increased by 150 % (Friedlingstein et al., 2024; Saunio et al., 2025). CH<sub>4</sub> is the most prevalent non-CO<sub>2</sub> greenhouse gas, with a warming potential 28 times that of CO<sub>2</sub> over 100 years and 84 times over 20 years. (Lee et al., 2023; Montzka et al., 2011; Saunio et al., 2016; Stocker et al., 2013) and an atmospheric lifetime of  $9.1 \pm 0.9$  years (Zhou et al., 2023; Saunio et al., 2025). Starting from 2007, the concentration of CH<sub>4</sub> has proliferated from an annual global mean of 1775 ppb to 1921 ppb in 25 2024, with a total rise of 146 ppb, which denotes a huge overall growth since the start of industrialization. The warming of wetlands, an increase in the ruminant population, and a decline in biomass burning, previously masking the rise in isotopically negative fuel use, are some of the key factors that may have contributed to the recent surge in CH<sub>4</sub> concentrations (Nisbet et al., 2019). The observed decline in carbon isotope ratio ( $\delta^{13}\text{CH}_4$ ) indicates a shift toward increasing biogenic CH<sub>4</sub> sources, such as microbial emissions from wetlands and agriculture (has a more negative  $\delta^{13}\text{CH}_4$  signature) rather than fossil fuel or 30 biomass burning contributions (Skeie et al., 2023; Schaefer et al., 2016). The long-term trend in OH remains uncertain, with some studies suggesting increases (e.g. Stevenson et al. (2020)), others finding no significant trend (Thompson et al., 2024), and still others showing diverging results depending on methodology (Saunio et al., 2025).

The global stock-take under Article 14 of the Paris Agreement implies the responsibility of each party to prepare, communicate, and maintain the successive nationally determined contributions (NDCs) to climate action (EC 2014). A 30 % global 35 reduction in CH<sub>4</sub> emissions from 2020 to 2030 has been aimed at the Global Methane Pledge, launched at a 2021 meeting of the United Nations Framework Convention on Climate Change (UNFCCC). Being one of the significant contributors to greenhouse gas (GHG) emissions, India plays an essential role in the global GHG scenario. Still, it lacks sufficient long-term, continuous, and accurate observations of the GHG to quantify the sources and sinks (Zhang et al., 2014). The country has the largest cattle (including bovine) population in the world citepRobinson2014Livestock. Along with this, its huge intense 40 flood irrigation practices, ever-increasing fuel demand, and large wetland extent (nearly 4.7 % of its total geographical area) contribute to its high CH<sub>4</sub> emission potential (Ganesan et al., 2017; Garg et al., 2011; Ministry of Environment and Change, 2015; Myhre et al., 2013b). CH<sub>4</sub> emissions from enteric fermentation account for about 8 % of the total GHG emissions of India's National GHG inventory 2020 (MoEFCC, 2024). The Emissions Database for Global Atmospheric Research (EDGAR) inventory provides a global sector-wise emission estimate for CH<sub>4</sub>. However, the bottom-up approach of EDGAR inventory 45 is limited by its accuracy and temporal resolution owing to uncertainties in the data used and methodologies (e.g. uncertain emission factors, aggregation or interpolation errors and sector distribution). Besides, Indian wetland emissions also show inconsistency in estimations ( $\sim 5$  to 9 %) depending on the wetland model used (Bloom et al., 2017). Janardanan et al. (2024)

reported large uncertainty in wetland emission inventory data over the Indian domain based on satellite observations and models. Further, insufficient coverage of highly precise and accurate ground-based observations of CH<sub>4</sub> and inadequate access to  
50 emission reporting over the country can lead to misrepresentations in global emission inventories.

Atmospheric concentration measurements contain integrated information on the underlying source-sink distribution. Therefore, integrating atmospheric mixing ratio measurements, flux information from bottom-up approaches, and transport model simulations can potentially enhance CH<sub>4</sub> estimates through inverse modeling (Bergamaschi et al., 2018) and independently evaluate reported flux estimates. Previous studies over India have been limited by coarse model resolution, incomplete repre-  
55 sentation of transport processes, or lack of high-resolution emission inventories. Due to these inadequate modeling systems and sparse ground measurements, limited studies have used atmospheric CH<sub>4</sub> observations to inform about CH<sub>4</sub> emission flux estimates across India. There is an urgent call for measurement that can sufficiently constrain regional emissions in modeling systems (Patra et al., 2016). Recent technological advancements in satellite remote-sensing enable high-resolution-high-density observations to be utilized for this inverse-based quantification when modeling techniques are adequately advanced (Myhre  
60 et al., 2013a; Jacob et al., 2016; Alexe et al., 2015; Buchwitz et al., 2017; Liang et al., 2023; Lu et al., 2022). Ganesan et al. (2017) used a top-down approach to estimate India's CH<sub>4</sub> emission for 2010-2015. The above study used column-averaged observations of CH<sub>4</sub> from the Greenhouse Gases Observing Satellite (GOSAT) along with aircraft observations from Civil Aircraft for the Regular Investigation of the Atmosphere Based on an Instrument Container (CARIBIC) and a few surface measurements from Indian sites to calculate methane emissions by atmospheric inverse modeling. Since 2009, GOSAT has  
65 measured the atmospheric column for CH<sub>4</sub> every three days at a 10 km diameter circle (Butz et al., 2011). Despite some limitations in temporal coverage, the spatial resolution of GOSAT observations is much better than its predecessor, the Scanning Imaging Absorption Spectrometer for Atmospheric Chartography (SCIAMACHY), which the research community has widely used (Butz et al., 2011; Yokota et al., 2009; Turner et al., 2015; Buchwitz et al., 2005; Schneising et al., 2011).

Since November 2017, the more recent TROPOspheric Monitoring Instrument (TROPOMI) on board the Copernicus Sentinel-  
70 5 Precursor satellite provides much higher-density CH<sub>4</sub> observations at a high spatial resolution of  $7 \times 7 \text{ km}^2$ , upgraded to  $5.5 \times 7 \text{ km}^2$  in August 2019 (Hu et al., 2018; Schneising et al., 2023). TROPOMI measures CH<sub>4</sub> at the  $2.3 \mu\text{m}$  band, with a swath width of 2600 km (Jacob et al., 2016; Cusworth et al., 2018). These observations are expected to capture seasonal fluctuations, which, in turn, will give better insight into the source-sink characteristics and quantification. Hence, in the present study, we explore the potential of TROPOMI measurements in representing the distribution of CH<sub>4</sub> fluxes over the Indian region along-  
75 side a spatio-seasonal analysis of the CH<sub>4</sub> bottom-up inventory information. We use TROPOMI XCH<sub>4</sub> for its dense, near-daily coverage over India, enabling higher comparability with the simulation of 10 km from our Weather Research and Forecasting

model coupled with the Chemistry and Greenhouse Gas module (WRF-GHG), which may effectively minimize the forward model-related uncertainties in the carbon assimilation system over India. The performance of this high-resolution model and the advantage of using highly resolved transport fields are previously reported in Thilakan et al. (2022) and Vellalassery et al. (2021). The assessment of the forward model, WRF-GHG, in the atmospheric boundary layer is performed by comparing the atmospheric CH<sub>4</sub> simulations with atmospheric measurements from a ground-based site. Finally, the annual CH<sub>4</sub> emission estimate is also derived for the period 2018-2019 by incorporating the TROPOMI measurements and WRF-GHG forward model in an atmospheric inversion algorithm. The overview of spatiotemporal analysis of methane-emission patterns across India from global bottom-up inventories, including agriculture, livestock, and fossil-fuel sectors and their impact on column-averaged methane mixing ratio enhancements, provides the context for improving or complementing current emission estimates over India.

The paper is organized as follows: Section 2 describes the data and methods used for the study. Section 3 presents data post-processing and inverse analysis, and Section 4 discusses the results of the study. The conclusions of the study are presented in Section 5.

## 2 Data and methods

In this section, we describe the measurements and techniques used for exploring the potential of TROPOMI measurements and the WRF-GHG atmospheric transport model in inferring CH<sub>4</sub> distribution over India. An inverse method has been devised to deduce the CH<sub>4</sub> fluxes over the Indian region by minimizing mismatches between TROPOMI CH<sub>4</sub> measurements and WRF-GHG mixing ratio simulations, thereby correcting the distribution of prior fluxes. Figure 1 shows the model domain with outlines of each geographical region (more details are given in the subsequent sections) considered in this study.

### 2.1 TROPOMI observations

The potential of TROPOMI Sentinel-5p to detect significant sources in the single overpass has been demonstrated in recent publications (Hu et al., 2018; de Gouw et al., 2020; Schneising et al., 2020; Chen et al., 2022; Jacob et al., 2022). We utilized TROPOMI CH<sub>4</sub> observations obtained through the Short Wave Infrared (SWIR) band, centered at approximately 2.3  $\mu\text{m}$ . The atmospheric column-averaged CH<sub>4</sub> mixing ratio ( $X_{\text{CH}_4}$ ) is retrieved using the Weighting Function Modified Differential Optical Absorption Spectroscopy (WFM-DOAS) algorithm. The WFMD algorithm uses a least-squares approach based on scaling prior atmospheric vertical profiles to retrieve  $X_{\text{CH}_4}$  and  $X_{\text{CO}}$  simultaneously (Buchwitz et al., 2007; Schneising et al., 2011). Here, we use the WFMD v1.8 algorithm, for which the efficiency has been validated using Total Carbon Column

Observing Network (TCCON) measurements, resulting in an improved random error (12.4 ppb) compared to the previous  
105 versions (v1.5 and v1.2) (Schneising et al., 2023). For the analysis, we filtered flagged data and utilized only good-quality  
retrievals represented by *xch4\_quality\_flag* = 0.

## 2.2 Modeling system for atmospheric XCH<sub>4</sub> mixing ratio simulations

We have used the Weather Research and Forecasting model coupled with the Chemistry and Greenhouse Gas module (hereafter  
referred to as WRF-GHG) for atmospheric CH<sub>4</sub> transport simulations. The core component is the WRF model, based on  
110 fully compressible, non-hydrostatic Eulerian equations on terrain-following vertical grids for simulating atmospheric transport  
(Skamarock et al., 2008). The GHG-TRACER package allows the online passive tracer transport of CH<sub>4</sub> mixing ratio in the  
atmosphere (Beck, 2011; Pillai et al., 2016). The input fluxes from each emission sector are separately provided as "tagged"  
tracers when added to the first layer in the modeling system. This allows the decoupling of emission contributions to the total  
atmospheric CH<sub>4</sub> mixing ratio. We have used the WRF-GHG 3.9.1.1 version with a horizontal resolution of  $10 \times 10$  km<sup>2</sup>  
115 (Lambert conformal conic projection grid) and an output temporal resolution of 1 hour. The model covers the Indian domain  
with  $307 \times 407$  grid points and 39 vertical levels. The fifth generation ECMWF reanalysis (ERA-5) data with a horizontal  
resolution of  $0.25^\circ \times 0.25^\circ$  and temporal resolution of 6 hours with 137 vertical levels are used as initial and boundary  
conditions for meteorology (Hersbach et al. (2020); see Table 1). The model is re-initialized each day with ERA5 meteorology,  
in which a 6-hour spin-up time was configured. For CH<sub>4</sub> mixing ratio fields, initial and boundary conditions are prescribed from  
120 the Copernicus Atmosphere Monitoring Service (CAMS re-analysis data). CAMS provides the simulated atmospheric mixing  
ratios of CH<sub>4</sub>, with a spatial resolution of  $0.25^\circ \times 0.25^\circ$  and a temporal resolution of 6 hours on 60 vertical levels (Inness  
et al. (2019); see Table 1). The model utilizes these initial fields to represent the background of the total mixing ratios. Similar  
to emission flux contributions, we disentangled the background contribution in the model output to investigate its impacts  
separately. We have also considered the reported level of uncertainties in CAMS-simulated mixing ratios (e.g. Agustí-Panareda  
125 et al. (2023); Wang et al. (2023)) and applied a monthly factor correction (1 to 3 % correction for the whole model domain) to  
our CAMS-simulated WRF-GHG background to minimize the unrealistic representation of background contribution to XCH<sub>4</sub>  
levels. The corrected WRF-GHG background mixing ratios are hereafter termed simply as background mixing ratios.

We used the Emission Database for Global Atmospheric Research (EDGAR v7.0; Crippa et al. (2024)), Global Fire Assimi-  
lation System (GFAS v1.2; Kaiser et al. (2012)), and a global wetland CH<sub>4</sub> emissions and uncertainty dataset for atmospheric  
130 chemical transport models (WetCHARTs 1.3.1; Bloom et al. (2021)) as prior emission fluxes to represent anthropogenic,  
biomass burning and wetland emissions respectively. We applied temporal scaling factors to the annual EDGAR emissions

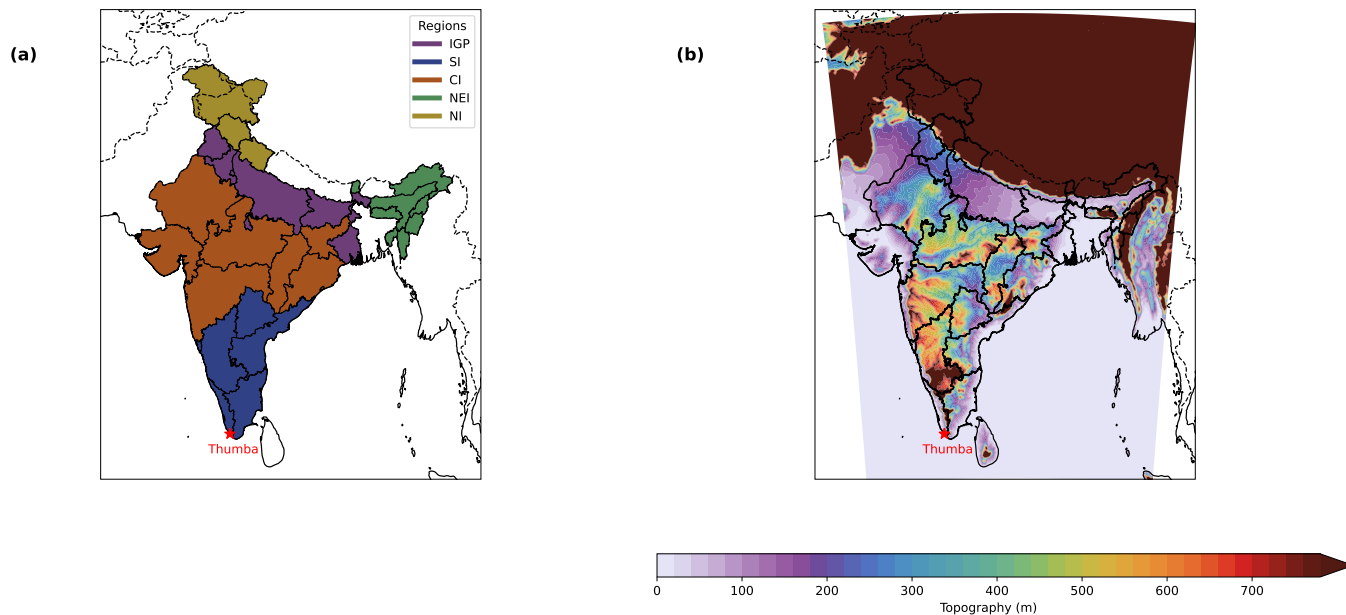


**Figure 1.** (a) Outlines showing each geographical region of the Indian landmass according to Survey of India (2024) and (b) the topographical height contour of the model domain. CI stands for Central India, NEI for North East India, NI for North India, SI for South India, and IGP for the Indo Gangetic Plain regions.

using step-function time profiles and converted them to 1-hour temporal resolution, following Kretschmer et al. (2014). GFAS data with  $0.1^\circ \times 0.1^\circ$  resolution represents biomass burning emissions in the model. GFAS emissions are calculated using fire radiative power observations from the Moderate Resolution Imaging Spectroradiometer (MODIS) instrument aboard the Terra satellite.

WetCHARTs is an ensemble dataset that provides gridded emissions data from 2001 to 2019 at a resolution of  $0.50^\circ \times 0.50^\circ$  (Bloom et al., 2017), which were then re-gridded to  $0.1^\circ \times 0.1^\circ$  with a temporal resolution of 1 hour. The simulated total atmospheric  $\text{CH}_4$  mixing ratio thus contains contributions from the initial fields as well as anthropogenic, biomass burning, and biogenic fields of  $\text{CH}_4$ . Table 1 summarizes the WRF-GHG model set-up used in this study. The general meteorological configuration for the WRF-GHG model set-up applied here is described in Thilakan et al. (2022).

**Table 1.** WRF-GHG model configuration.

<b>Parameter</b>	<b>Details</b>
Domain Configuration	Single domain with a horizontal resolution of 10 km; 39 vertical levels; 307 × 407 grid points
Vertical coordinates	Terrain-following hydrostatic pressure vertical coordinates
Basic equations	Non-hydrostatic; compressible
Grid type	Arakawa C grid
Time integration	Third-order Runge–Kutta split explicit
Spatial integration	Third- and fifth-order differencing for vertical and horizontal advection, respectively; both for momentum and scalars
Time step	60 s
Model top pressure	50 hPa
Physics schemes	
<i>Radiation</i>	Rapid Radiative Transfer Model (RRTM) for longwave and Dudhia for shortwave
<i>Microphysics</i>	WRF single-moment three-class (WSM3) classic simple ice scheme
<i>PBL</i>	Yonsei University (YSU) scheme
<i>Surface layer</i>	Monin–Obukhov
<i>Land surface</i>	NOAH land surface model (LSM)
<i>Cumulus</i>	Grell–Freitas ensemble scheme
Emission fields	
<i>Flux type</i>	Product Version Spatial res. Temporal res. Source/website Reference
<i>Anthropogenic</i>	EDGAR v7.0 10 km Annual <a href="https://edgar.jrc.ec.europa.eu/">https://edgar.jrc.ec.europa.eu/</a> (Crippa et al., 2024)
<i>Biomass burning</i>	GFAS v1.2 10 km Daily <a href="http://apps.ecmwf.int/datasets/data/cams-gfas/">http://apps.ecmwf.int/datasets/data/cams-gfas/</a> (Kaiser et al., 2012)
<i>Biospheric</i>	WetCHARTs V1.3.1 0.5° Monthly <a href="https://daac.ornl.gov/cgi-bin/dsviewer.pl?ds_id=1915">https://daac.ornl.gov/cgi-bin/dsviewer.pl?ds_id=1915</a> (Bloom et al., 2017)
Initial and lateral boundary conditions	Product Version Spatial res. Temporal res. Source/website Reference
<i>Field</i>	ERA5 NA 25 km 1 h <a href="https://cds.climate.copernicus.eu/cdsapp#!home">https://cds.climate.copernicus.eu/cdsapp#!home</a> (Hersbach et al., 2020)
<i>Meteorology</i>	ECMWF/CAMS EGG4 50 km 6 h <a href="http://atmosphere.copernicus.eu">http://atmosphere.copernicus.eu</a> (Agusti-Panareda et al., 2023)
<i>Tracer</i>	

### 2.3 Ground-level observations

To assess the model's performance at the surface level, a comparative analysis was conducted using CH<sub>4</sub> *in situ* measurements from a ground-level pollution monitoring station in Thumba (8.5°N, 76.9°E) as denoted in Fig. 1 for 2018 & 2019. Located in southwestern India, Thumba is a tropical coastal station approximately 10 km northwest of Thiruvananthapuram and 500 m inland from the Arabian Sea. This site reflects local to regional influences, but cannot capture the full spatial variability across India. CH<sub>4</sub> concentrations were measured using a greenhouse gas analyzer (model: 911-0011-1001) by Los Gatos Research, USA, based on the off-axis integrated cavity output spectroscopy (OA-ICOS) method (Baer et al., 2002; Raju et al., 2022; Sijikumar et al., 2023; Uma et al., 2024). Air samples were collected from about 10 m above ground level (AGL) using the analyzer's internal pump. Calibration was performed periodically. However, it should be noted that the instrument can be sensitive to temperature, requiring frequent calibration, which was not regularly met. Measurements were recorded at 1-second intervals, with hourly averages used for subsequent analysis. CH<sub>4</sub> measurement uncertainty is 0.25 % (i.e. 5 ppb with respect to 2000 ppb of CH<sub>4</sub>) and the reported precision ( $1 \sigma$ ) is 1 ppb.

### 2.4 Data post-processing and inverse analysis

We regridded the daily total dry column mixing ratio of CH<sub>4</sub> from TROPOMI at  $0.10^\circ \times 0.10^\circ$  resolution, covering a period of 2018 to 2019. From the hourly WRF-GHG CH<sub>4</sub> mixing ratio simulations generated, we sampled those corresponding to the TROPOMI overpass time for the model domain. The model top is restricted to  $\sim 50$  hPa (model top pressure), and the model does not take into account stratospheric CH<sub>4</sub> chemistry, which is expected to make a negligible impact on total column averages of CH<sub>4</sub> during the analysis time, considering the methane lifetime in the stratosphere. However, to ensure a fair comparison with observations, we applied the satellite's averaging kernel (AK), as shown in Equation 1, by considering the vertical sensitivity of the satellite instrument (Schneising et al., 2019). AK is proportional to the sensitivity profile of the measurement that is weighted with the assumed tracer profiles and provides the relation between the retrieved and known tracer profiles. i.e. Applying satellite AK to the model simulations at different vertical levels minimizes the mismatches owing to the instrument vertical sensitivities to the column observations (Eskes and Boersma, 2003; Wang et al., 2023; Schneising, 2024).

We applied the AK to the modeled dry-air CH<sub>4</sub> profiles and derived the dry-air column-averaged mixing ratio of CH<sub>4</sub>,  $\Upsilon_{\text{mod}}$ , as follows:

$$\Upsilon_{\text{mod}} = \sum_l (\Upsilon_{\text{apr}}^l + A_l (\Upsilon_{\text{mod}}^l - \Upsilon_{\text{apr}}^l)) w_l \quad (1)$$

where  $l$  is the index of the vertical layer,  $A_l$  is the averaging kernel and  $\Upsilon_{\text{apr}}^l$  is the *a priori* mole fraction of layer  $l$ , and  $\Upsilon_{\text{mod}}^l$  is the corresponding simulated mole fraction of layer  $l$ .  $w_l$  is the layer-dependent pressure weight.

170 Hence,  $\Upsilon_{\text{mod}}$  ( $= \text{XCH}_{4,\text{mod}}$ ) is used for the model-observation comparisons and inversion analyses. i.e., in this study,  $\Upsilon_{\text{mod}}$  represents WRF-GHG  $\text{XCH}_4$  simulations.

### 2.4.1 Estimating optimized $\text{CH}_4$ flux over India

We performed a simple Bayesian inverse optimization to deduce the improved emission estimates over the Indian domain. The inversion is designed in such a way that it describes the relationship between the mixing ratio observations and the surface flux emission information (the unknown state) and *a priori* information available. This approach allows us to identify 175 the class of possible states consistent with the available information and to assign a probability density function (pdf) to them. The quantities to be optimized, represented by the state vector  $\mathbf{x}$  with  $n$  elements  $x_1, x_2, x_3, \dots, x_n$  correspond to the monthly, state-wise emissions from (i) anthropogenic components (EDGAR) and (ii) the sum of anthropogenic (EDGAR) and biomass-burning (GFAS) components, both (i) and (ii) optimized separately. We have omitted the wetland component here since it contributed negligibly to the column-mixing-ratio enhancement. Here,  $n$  represents 36 state regions of India. 180 The measured quantities, represented by the measurement vector  $\mathbf{y}$  with  $m$  elements  $y_1, y_2, y_3, \dots, y_m$ , represent the total column observations from TROPOMI over a month at  $0.1^\circ \times 0.1^\circ$  spatial resolution. Here,  $m$  represents the total number of observations available in each political state.

The relationship between the measurement vector,  $\mathbf{y}$ , and the state vector,  $\mathbf{x}$ , can be written as:

$$185 \quad \mathbf{y} = \mathbf{F}(\mathbf{x}) + \epsilon \quad (2)$$

where  $\mathbf{F}(\mathbf{x})$  encapsulates the physics of the measurements as a function of the state vector, described here by our forward model, WRF-GHG, which includes forward transport and mapping of flux fields. The error term  $\epsilon$  includes model error, representation error (sampling mismatch between the observations and the model), and measurement error.

Linearizing the forward model to a reference state yields:

$$190 \quad \mathbf{F}(\mathbf{x}) = \mathbf{K}\mathbf{x} + \boldsymbol{\epsilon} \quad (3)$$

Here,  $\mathbf{K}$  is the  $m \times n$  Jacobian matrix, representing the sensitivity of the mixing ratio simulated by the forward model to the state vector. The elements of  $\mathbf{K}$  are thus:  $k_{m,n} = \frac{\partial \mathbf{F}_m(\mathbf{x})}{\partial x_n}$

Since we have not implemented the adjoint model for our forward transport model, the Jacobian was constructed by applying the transport model (WRF-GHG) to perturbed emissions over the target region (each political state) and obtaining the sensitivity  
195 to the corresponding observations, as follows:

$$\mathbf{K} = \frac{(\boldsymbol{\Upsilon} + \Delta \boldsymbol{\Upsilon}) - \boldsymbol{\Upsilon}}{\sum_{\text{TR}} \boldsymbol{\Phi}_{\text{perturbed}} - \sum_{\text{TR}} \boldsymbol{\Phi}} \quad (4)$$

Here,  $\boldsymbol{\Upsilon}$  is the column mixing ratio field, and  $(\boldsymbol{\Upsilon} + \Delta \boldsymbol{\Upsilon})$  is the perturbed column mixing ratio field over the target region.  $\boldsymbol{\Phi}$  is the emission flux field, and  $\boldsymbol{\Phi}_{\text{perturbed}}$  is the perturbed emission flux field over the target region (TR).

In our implementation, we focus on anthropogenic fluxes and their contributions to the atmospheric dry air column mixing  
200 ratios.  $\mathbf{x}_A$  represents the prior fluxes, which consist of monthly anthropogenic (major contributions from enteric fermentation, agricultural soil, waste water handling, and fuel exploitation) and biomass burning emissions. For the optimization, we average the emissions per state. i.e. optimizing one parameter per state representing the total emissions for that state. The background contributions are removed from the observations to optimize the regional enhancement fluxes. i.e., the measurement vector  $\mathbf{y}$  consists of total column observations from TROPOMI subtracted by simulated background mixing ratios over a month at  
205  $0.1^\circ \times 0.1^\circ$  spatial resolution.

The background mixing ratios are simulated by WRF-GHG, as explained in Sect. 2.2. We have considered measurement errors (including forward model errors) and prior errors:  $\mathbf{S}_e$  and  $\mathbf{S}_a$  represent measurement error and prior error covariance matrices, respectively. The measurement error covariance matrix  $\mathbf{S}_e$  consists of  $\text{CH}_4$  retrieval ( $\mathbf{y}$ ) and the forward model ( $\mathbf{F}(\mathbf{x})$ ) errors. We assumed a prior emission uncertainty of 80% and a measurement uncertainty of 16 ppb, as adopted from Liang et al.  
210 (2023), calculated using the residual error method (Heald et al., 2004). We have not considered cross-correlations; hence, only the diagonal elements of the matrices  $\mathbf{S}_e$  and  $\mathbf{S}_a$  are non-zero. The chosen measurement uncertainty encompasses the variability across TROPOMI  $\text{XCH}_4$  products ( $\leq 16$  ppb; see Fig. S1). Nonetheless, as illustrated in Fig. S1, systematic differences exist among  $\text{XCH}_4$  products, which are likely to impact the optimization of fine-scale state vectors. Understanding how differences

in various retrieval products influence flux estimations is vital for characterizing posterior uncertainty in inverse studies. This  
 215 necessitates a more sophisticated inverse configuration that also includes a higher discretization of state space and a detailed  
 sensitivity analysis of prior and posterior fluxes across the region, which we consider as a future direction for this study.  
 However, we considered the systematic observational differences due to different retrieval algorithms, as seen in Fig. S1, in a  
 separate inversion by redefining the measurement uncertainty (>50 % more than the originally defined, ~ 25 ppb) that more or  
 less represents the worst case scenario for retrieval differences across the region. The above setup can thus allow us to examine  
 220 the maximum likelihood impact of such retrieval differences on posterior flux estimates at a national scale.

The solution to the inverse problem is obtained by minimizing the Bayesian scalar cost function  $J(\mathbf{x})$  (Rodgers, 2000):

$$J(\mathbf{x}) = (\mathbf{x} - \mathbf{x}_A)^T \mathbf{S}_a^{-1} (\mathbf{x} - \mathbf{x}_A) + (\mathbf{y} - \mathbf{K}\mathbf{x})^T \mathbf{S}_e^{-1} (\mathbf{y} - \mathbf{K}\mathbf{x}_A) \quad (5)$$

where  $\nabla_{\mathbf{x}} J(\mathbf{x}) = 0$ , the optimal estimate  $\hat{\mathbf{x}}$  is obtained (Rodgers, 2000). The state that maximizes the posterior pdf  $P(\mathbf{x}|\mathbf{y})$  is  
 the maximum a posteriori solution (MAP). The maximum a posteriori solution is obtained as follows:

$$225 \quad \hat{\mathbf{x}} = \mathbf{x}_A + \left( \mathbf{K}^T \mathbf{S}_e^{-1} \mathbf{K} + \mathbf{S}_a^{-1} \right)^{-1} \mathbf{K}^T \mathbf{S}_e^{-1} (\mathbf{y} - \mathbf{K}\mathbf{x}_A) \quad (6)$$

Thus,  $\hat{\mathbf{x}}$  represents the optimized spatially averaged monthly anthropogenic and biomass burning fluxes corresponding to  
 each political state considered. The posterior error covariance matrix, denoted by  $\hat{\mathbf{S}}$ , is derived as follows.

$$\hat{\mathbf{S}} = (\mathbf{K}^T \mathbf{S}_e^{-1} \mathbf{K} + \mathbf{S}_a^{-1})^{-1} \quad (7)$$

The error reduction for each month following the inversion procedure ( $\tilde{e}$ ) is calculated as follows:

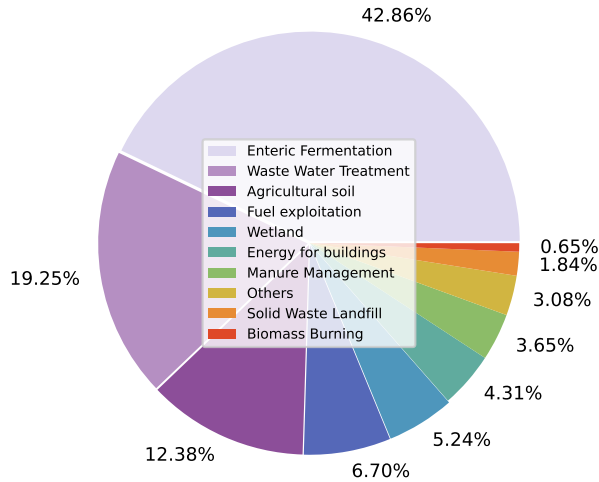
$$230 \quad \tilde{e} = 1 - \frac{\sigma_{post}}{\sigma_{prior}} \quad (8)$$

where  $\sigma_{post}$  is derived as the square root of the diagonal elements of  $\hat{\mathbf{S}}$ . Similarly,  $\sigma_{prior}$  is obtained from the square root of  
 the diagonal elements of the prior error covariance matrix.

The national budget for annual optimized fluxes  $\hat{\mathbf{x}}_{annual}$  (in Tg  $y^{-1}$ ) is derived as:

$$\hat{\mathbf{x}}_{annual} = \sum_{t=1}^{N_t} \sum_{s=1}^{N_s} \hat{\mathbf{x}}_{s,t}, \quad (9)$$

(a)



(b)

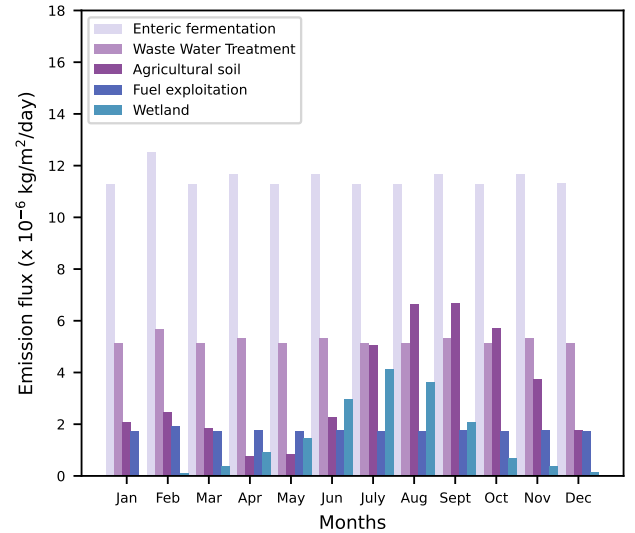


**Figure 2.** (a) The percentage of contributions of different CH<sub>4</sub> sources towards total annual emission flux over the Indian domain, (b) monthly contribution (calculated from the EDGAR temporal profiles described in Crippa et al. (2020)) from each source.

235 where  $\hat{x}_{s,t}$  represents the estimated value at each political state  $s$  for the corresponding month  $t$ .  $N_s$  is the total number of political states, and  $N_t$  is the total number of months considered.

### 3 Results and Discussion

#### 3.1 Regional and sectoral distribution of CH<sub>4</sub> sources

240 The bottom-up inventories such as EDGAR v8.0 (latest release; Crippa et al. (2024)), WetCHARTs v1.3.1, and GFAS v1.2. relate the GHG emissions to the causative processes by considering emission activities and emission factors, thereby providing us with a "first guess" to identify the prominent sources (Miller and Michalak, 2017), although with inherent uncertainties. In this section, we present a detailed comparative assessment of the sectoral and regional distributions of different CH<sub>4</sub> sources (such as enteric fermentation, wastewater handling, rice agricultural land, wetlands, and biomass burning).

245 Our sector-wise analysis of the bottom-up inventories shows that the enteric fermentation associated with the digestive process in cattle makes a significant contribution to CH<sub>4</sub> emissions in India (42.9 %), followed by wastewater treatment (19.2 %), agricultural soil (12.4 %), fuel exploitation (6.7 %), and wetland (5.2 %, excluding agriculture) (see Fig.2). The sources with significant seasonality include agriculture (see Fig.2 (b)) and biomass burning, also reported in Ganesan et al. (2017).

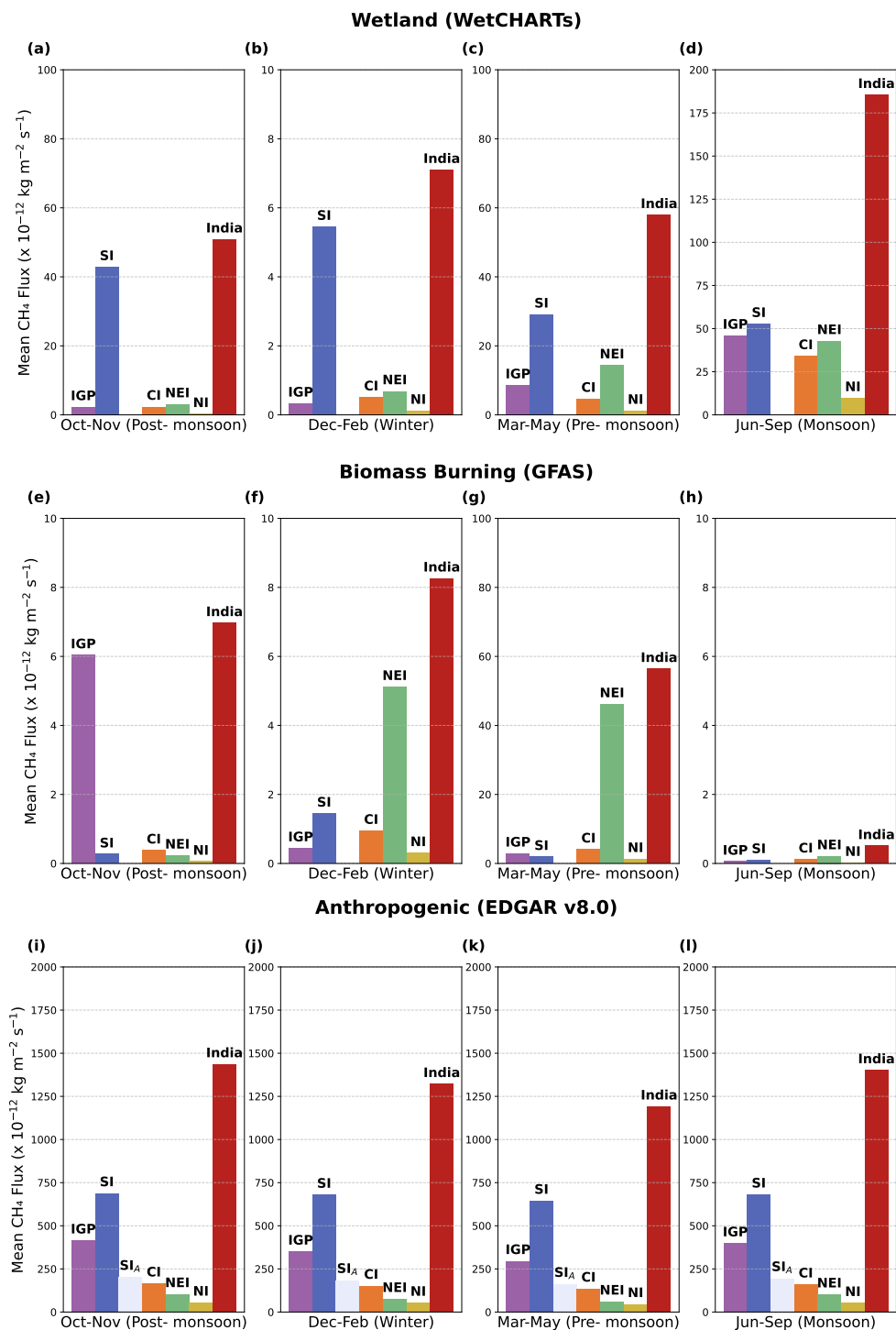


**Figure 3.** Seasonal mean emissions from (top panels) wetland, (middle panels) biomass burning, and (bottom panels) anthropogenic sources, separated for seasons, for each region as specified in Figure 1. Note: The ranges of the y-axes are not uniform in panels to improve visibility.

Figure S2. (a)-(d) shows an annual average of the spatial distribution of CH<sub>4</sub> emissions for the four major emission sectors in 2018. Anthropogenic sources are expected to provide the bulk of India's CH<sub>4</sub> emissions, especially livestock, rice cultivation, and waste management (Maasackers et al., 2019). The annual CH<sub>4</sub> emissions corresponding to rice cultivation (emission from the sector 'Agricultural soil' as given by the EDGAR inventory) show a peak in values over the Indo-Gangetic Plain (IGP) region (Fig.S2 (c)). Several other studies have used GOSAT and other data sources to analyse the CH<sub>4</sub> emissions from rice paddies in India (Miller et al., 2019; Ganesan et al., 2017; Anand et al., 2005). Previous studies reported CH<sub>4</sub> emissions from rice paddies in India of about 3.9 Tg yr<sup>-1</sup>, with the bulk emitted between June and September (Janssens-Maenhout et al., 2011; Garg et al., 2011; Panigrahy et al., 2010). The sector-wise analysis of the EDGAR inventory for the year 2018 shows significant CH<sub>4</sub> highs on the eastern coast, including West Bengal and Odisha, which can be attributed to the large rice cultivation in these regions (Crippa et al., 2023). The analysis of monthly emissions from rice cultivation over the year 2018 indicates an increasing pattern in summer monsoon seasons, June to September (see "Agricultural soil" in Fig. 2 (b)), with the maximum in August (16.9 %) and September (16.5 %) and the minimum in April (1.9 %); percentages are shares of the annual flux. There is a smaller peak in February-March time, owing to winter rice cultivation, which comprises 14 % of total rice production in India (Manjunath et al., 2006). Similarly, in the wetland emissions, we also see an increase in monsoon months (Fig. 2 b). The peak wetland emissions are seen in July (24.6 %), followed by August (21.4 %), and the minimum in January (0.2 %). It has been previously reported from satellite observations that the waterlogged areas increase nearly threefold from the beginning to the end of the monsoon, resulting in higher wetland CH<sub>4</sub> emissions (Agarwal and Garg, 2009). The pre-monsoon CH<sub>4</sub> emission (15.5 %) is higher than post-monsoon (6.2 %; see Fig. 2 (b), possibly due to higher temperatures during the pre-monsoon season as described in Das et al. (2023). Our analysis of monthly emissions based on GFAS shows a peak due to biomass burning in March (65.4 %), with the lowest burning reported in July (0.1 %) ( Fig. 3 (e)-(h)). Other sources of CH<sub>4</sub>, including fossil-fuel emissions, enteric fermentation, and wastewater handling, have not shown considerable seasonal variability. A similar pattern has also been observed from the 2019 anthropogenic and natural CH<sub>4</sub> emission analysis (figure not shown).

Further, the anthropogenic emissions remain the largest contributors to regional CH<sub>4</sub> emissions (see Fig. 3 & S3). The total anthropogenic emissions, reported by the EDGAR bottom-up inventory (version 8), peak seasonally in the South India (SI) region ( $> 700 \times 10^{12} \text{ kg m}^{-2} \text{ s}^{-1}$ ), followed by IGP ( $> 400 \times 10^{12} \text{ kg m}^{-2} \text{ s}^{-1}$ ), with the minimum emissions observed in North India (NI; see Fig. 3). The peak is typically in October-November, followed by June-September, with a minimum in March-May. Total anthropogenic emissions over India show a peak in October-November and a dip in March-May ( $1410- 1090 \times 10^{12} \text{ kg m}^{-2}$ ). While IGP shows high magnitude in spatial distribution (see Fig. S2 (a)-(d)), SI contributes more emissions due to emission hotspots. Four hotspots identified (see Fig. S5) in SI include one city- Namakkal ( $11.25^\circ N$ ,  $78.15^\circ E$ ; HS1) and three

villages- Mandapaka Rural (16.75 °N, 81.65 °E; HS2), Pasumamla (17.35 °N, 78.65 °E; HS3), and Mulkalappalli (18.65 °N, 79.55 °E; HS4). Excluding these hotspots (SI<sub>A</sub>) shifts the highest emissions to IGP (see Fig. 3 (i)-(l)). Namakkal in Tamil Nadu faces poultry waste deposition, potentially increasing methane emissions (Ramasamy and Manivel, 2019). Mandapaka in Andhra Pradesh, known as the "rice bowl" of the region, contributes to higher agricultural rice emissions (Gururaj Katti et al., 2002). Pasumamla in Telangana sees significant poultry waste dumping in landfills (<https://rangareddy.telangana.gov.in/animal-husbandry>, accessed 12 Feb 2025). Mulkappalli, a coal mining site in Telangana, contributes to the high CH<sub>4</sub> levels in the inventory (<https://khammam.telangana.gov.in/economy>, accessed 12 Feb 2025). Figure S6 shows the methane hotspots over the Indian domain from the coal mining sector as derived from the EDGAR inventory.

Based on WetCHARTs (version 1.3.1), natural wetland emissions are approximated at 1.7 Tg yr<sup>-1</sup>, with peak emissions occurring from June to September ( $\sim 185 \times 10^{12}$  kg m<sup>-2</sup>). The highest wetland emissions ( $>25 \times 10^{12}$  kg m<sup>-2</sup> s<sup>-1</sup>) are seen over the SI region in June-September, October-November, and March-May, with a peak of  $\sim 50 \times 10^{12}$  kg m<sup>-2</sup> s<sup>-1</sup> (Fig. 3). These peaks are likely due to increased waterlogged areas during the monsoon (Fig. 2b). Biomass burning emissions, smaller than wetland and anthropogenic emissions, peak in March-May in most regions except the IGP, where crop residue burning occurs from October to November (Deshpande et al., 2022, 2023). The North East India (NEI) region shows the highest biomass burning emissions in March-May ( $\sim 47 \times 10^{12}$  kg m<sup>-2</sup>), likely due to slash-and-burn practices before planting (Deshpande et al., 2023). Total emissions, combining anthropogenic (EDGAR), wetland (WetCHARTs), and biomass burning (GFAS) emissions, peak in October-November and June-September, with the SI region contributing the highest share (49.2 % and 46.4 %, respectively), and 52 % in March-May and 51.7 % in December-February.

Though the above estimations give an overview of Indian CH<sub>4</sub> source contributions and their regional patterns, there have been increased concerns about their accuracy due to methodological weaknesses and data gaps (Solazzo et al., 2021; Madrazo et al., 2018). For example, the combined emissions from Oil, Gas, and Coal over the Indian region reported by Scarpelli et al. (2025) is 1.8 Tg yr<sup>-1</sup>, whereas EDGAR reported 2.2 Tg yr<sup>-1</sup>. Also, bottom-up methods can overestimate or misinterpret emission sources even at the global level (Saunio et al., 2016). Though inverse modeling can improve the CH<sub>4</sub> budget significantly, its potential to minimize biases in the bottom-up models used as prior estimates may be limited by insufficient coverage of mixing ratio observations and its inadequate representation in the forward models. Satellite instruments such as TROPOMI may aid in high observation density with good spatial coverage (Palmer et al., 2021), the potential of which in the Indian context is explored in further sections.

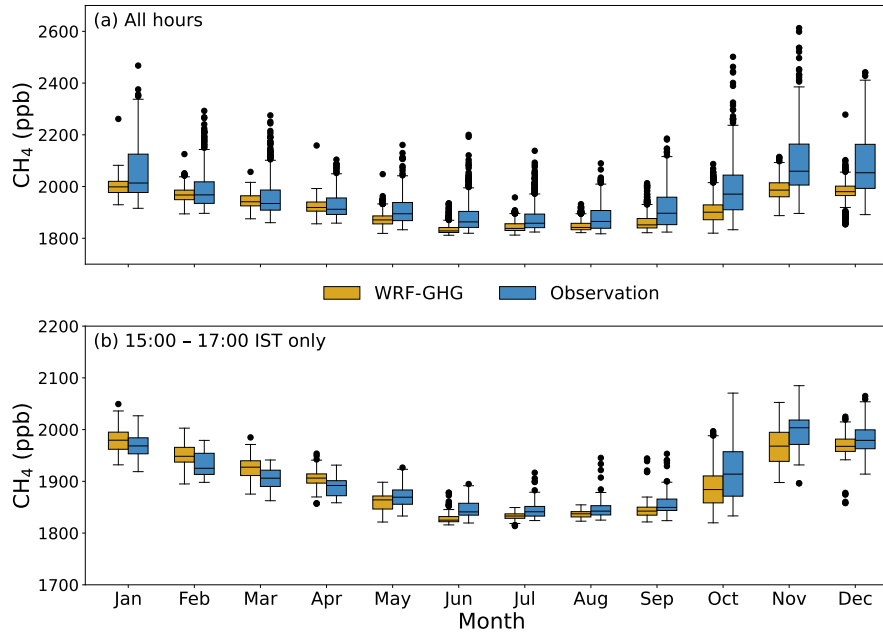


**Figure 4.** Monthly distribution of observed and WRF-GHG simulated CH<sub>4</sub> mixing ratios at Thumba for 2018 & 2019 for (a) all hours and (b) only 15:00 - 17:00 Local Time (IST hours) (25<sup>th</sup> and 75<sup>th</sup> quartiles; see the site location as denoted in Fig. 1). Note that the ranges of the y-axes are not uniform in panels to improve visibility.

### 3.2 Assessment of the forward-model performance against surface measurements

305 As discussed in Section 2.3, we utilized hourly ground-based observations from a ground-based site, Thumba, to assess the WRF-GHG performance in the planetary boundary layer. The lowest level (approximately 35.2 m) of WRF-GHG-simulated CH<sub>4</sub> at Thumba is compared with surface-level observations of CH<sub>4</sub> and is presented here. Generally, the analysis indicated a reasonable performance of WRF-GHG simulations. CH<sub>4</sub> mixing ratios are found to be lowest during the monsoon season (June–August), increasing from early October and peaking during the post-monsoon and winter months (November–January; see Fig. 4a). The maximum values are seen in December (~ 2100 ppb). The hourly observations show high variability (about 112.7 ppb), but ranging from 1817.4 to 2612.6 ppb for 2018-2019; see Fig. S7. Despite some discrepancies, the WRF-GHG simulations broadly align with those highly fluctuating observation patterns, capturing about 56 % of the observed variability. In October, monthly averaged WRF-GHG simulations and TROPOMI observations are strongly correlated, although their absolute values differ substantially (Figure not shown). The mean difference between observations and simulations is 47 ppb, but it shows large model-observation variability of up to 73.9 ppb (Fig. 4(a) and Fig. S7(a)). But, this large discrepancy between the model and observation can be caused by the influence of the fine-scale nocturnal coastal meteorological conditions prevail-

315

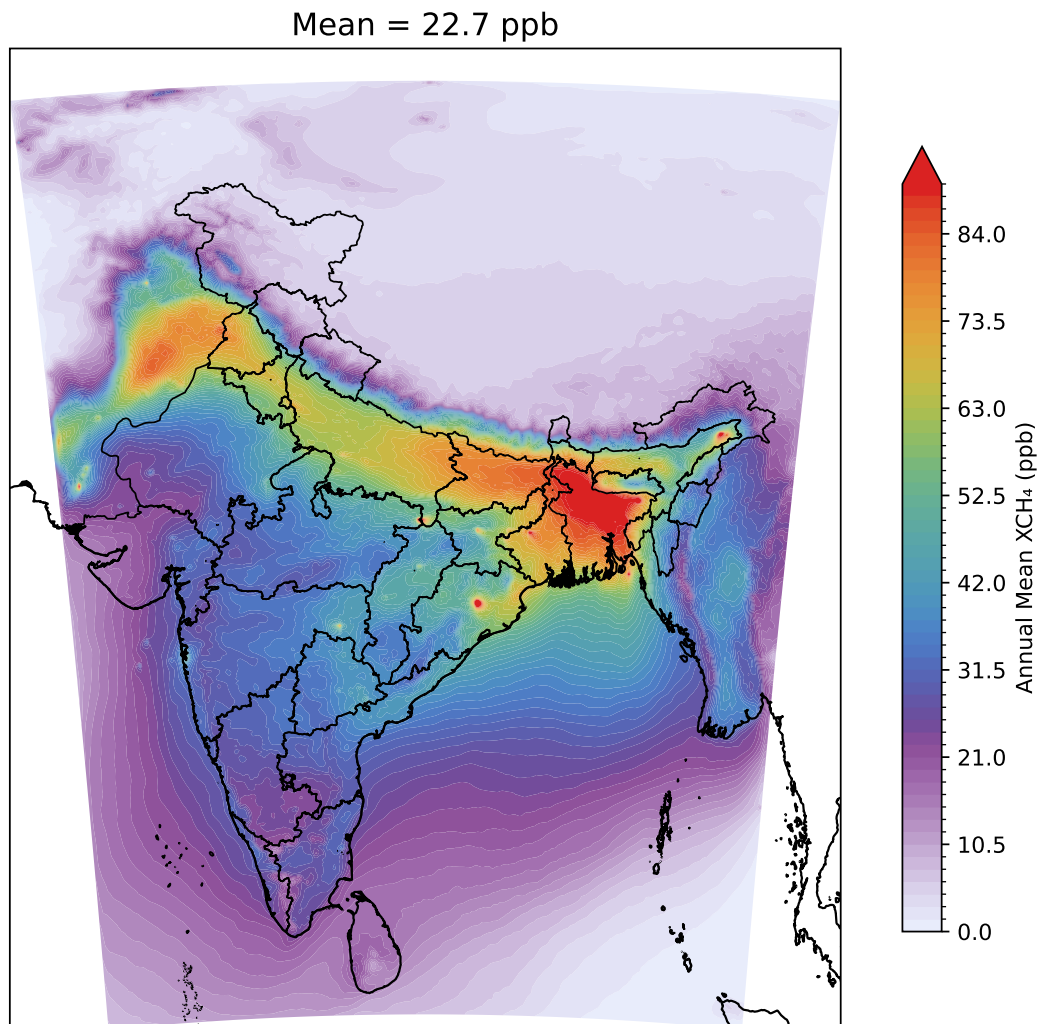


**Figure 5.** Spatial distribution for annual WRF-GHG simulated anthropogenic mixing ratio enhancement of XCH<sub>4</sub> (including biomass burning) for 2018.

ing in the measurement site as reported in Kavitha et al. (2018). Considering only the afternoon hours, the model-observation differences are reduced to 6.4 ppb, with a maximum difference varying up to 28.1 ppb, capturing about 79 % of observed variability (Fig. 4(b) and Fig. S7(b)). The comparison has also been done by removing the boundary contributions from CAMS  
 320 (see Fig. S8), showing that enhancements correlate ( $R^2=0.48$ ) with observed variability. Thus, the above comparison suggests the potential of our model in representing the regional and seasonal variations. The above result is promising, confirming the usability of those afternoon measurements representing well-mixed atmospheric conditions, which can be utilized for future carbon assimilation systems in conjunction with a high-resolution forward modeling framework. As seen for all hours,

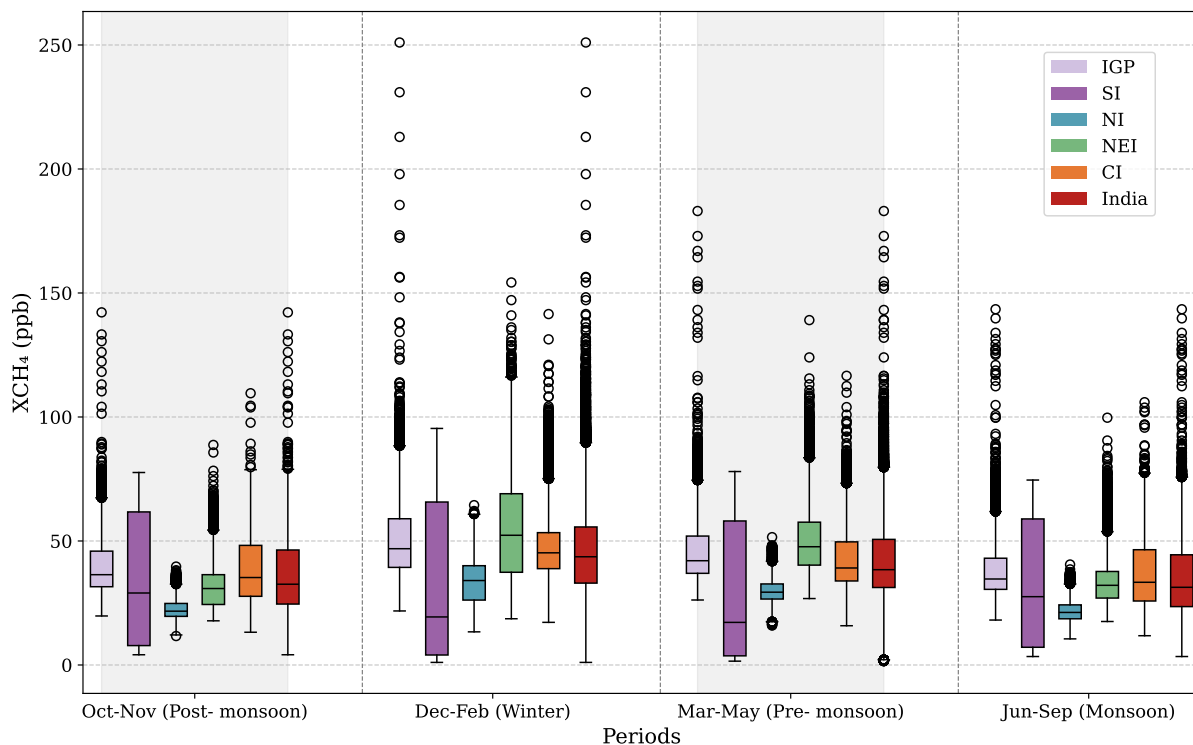


**Figure 6.** Distribution of seasonal average of simulated mixing ratio enhancement ( $XCH_{4,ant} + XCH_{4,bbu}$ ) over different regions of India in 2018. The box plot displays medians, interquartile ranges, and minimum and maximum values, with data points beyond 1.5 times the interquartile range represented as outliers.

WRF-GHG generally underestimates surface  $CH_4$  mixing ratios (Fig. S7). Notably, the model-observation differences peaked  
 325 in winter, owing to the unusually high variability seen in the observations during this period. The effect of enhanced vertical mixing can be seen in the summer months, causing low observed  $CH_4$  magnitude and associated mixing ratio variability. Noteworthy is that the magnitude of observed  $CH_4$  is found to be the smallest during the summer monsoon. While the shallow planetary boundary layer (PBL) in the winter accumulates the effect of surface emissions to the lower boundary, increased boundary layer mixing in the summer can cause lower  $CH_4$  magnitude and variability. Further, Guha et al. (2018) and Metya  
 330 et al. (2021) report that the influx of clean air from the Southern Hemisphere, carried by the monsoonal south-westerly winds, can influence the surface  $CH_4$  to lower its concentration. The high rates of OH radical oxidation may also influence surface  $CH_4$  mixing ratios (Lin et al., 2015).

Even though WRF-GHG has shown reasonable performance while evaluating the ground-based observations from a complex site (located near the southernmost coastal boundary of the model domain), the robustness of the model needs to be

335 further examined with multiple locations across India when they are available. Those evaluations are particularly necessary for assessing our confidence in the derived posterior fluxes.

### 3.3 Anthropogenic XCH<sub>4</sub> mixing ratio enhancements

In this section, we discuss the mixing ratio enhancements in the atmospheric column in response to spatial and temporal distributions of regional sources for the period 2018-2019. i.e. by considering only contributions from the sum of anthropogenic and biomass-burning emission sources (mostly human-influenced in India, i.e, from agricultural residue burning and managed fires) over the model domain and not using CAMS-derived background XCH<sub>4</sub> (see section 2.2). As mentioned in section 2.4.1, we have also omitted the wetland (biogenic) component here since it contributed negligibly to the column-mixing-ratio enhancement (see Fig. S10). The IGP region exhibits significant XCH<sub>4</sub> enhancements (from 27 ppb to 67 ppb) from regional sources attributed to anthropogenic and biomass-burning fluxes (see Figs. 5). Seasonally, the highest XCH<sub>4</sub> enhancements occur during winter (with a maximum of ~ 251 ppb in January; see Fig. S9) over India. The minimum enhancement for the whole Indian domain occurs during the monsoon season (June–September), likely due to a combination of higher boundary layer heights and stronger winds, which enhance vertical and horizontal transport affecting column CH<sub>4</sub> concentrations. The concentrations may also be impacted by the seasonal changes in regional or larger fluxes (>1000 km); however, further investigation is needed to assess their contributions.

350 Figure 6 (also see Fig. S11) shows the regional variability of anthropogenic XCH<sub>4</sub> enhancements across different parts of India as shown in Fig. 1. The highest regional magnitudes and variability in mixing ratio enhancements occur in the winter season. Here, consistently high magnitude in spatial distribution is found over the IGP region (with a median of ~ 50 ppb), showing maximum values over the SI region (~ 90 ppb) owing to emission hotspots. During winter, the NEI shows high XCH<sub>4</sub> enhancements, with values reaching up to 115 ppb (with a median value of ~ 60 ppb). Winter peaks in XCH<sub>4</sub> likely arise from stable atmospheric transport that carries and concentrates emissions from the preceding October–November period. From June to September, SI enhancements reach up to ~ 75 ppb (with a median value of ~ 25 ppb). A similar trend is seen for 2019 (Figure not shown). SI exhibits the widest interquartile range with the lowest minimum value, a relatively low median, and the highest maximum in most seasons, indicating the influence of hotspot emissions, as discussed earlier in Section 4.1.

### 3.4 Comparison of modeled and observed total XCH<sub>4</sub>

360 In this section, we present our comparisons of WRF-GHG simulations with TROPOMI observations of total XCH<sub>4</sub> in 2018, considering all months in which reasonable amounts of satellite measurements are available after filtering. The details of

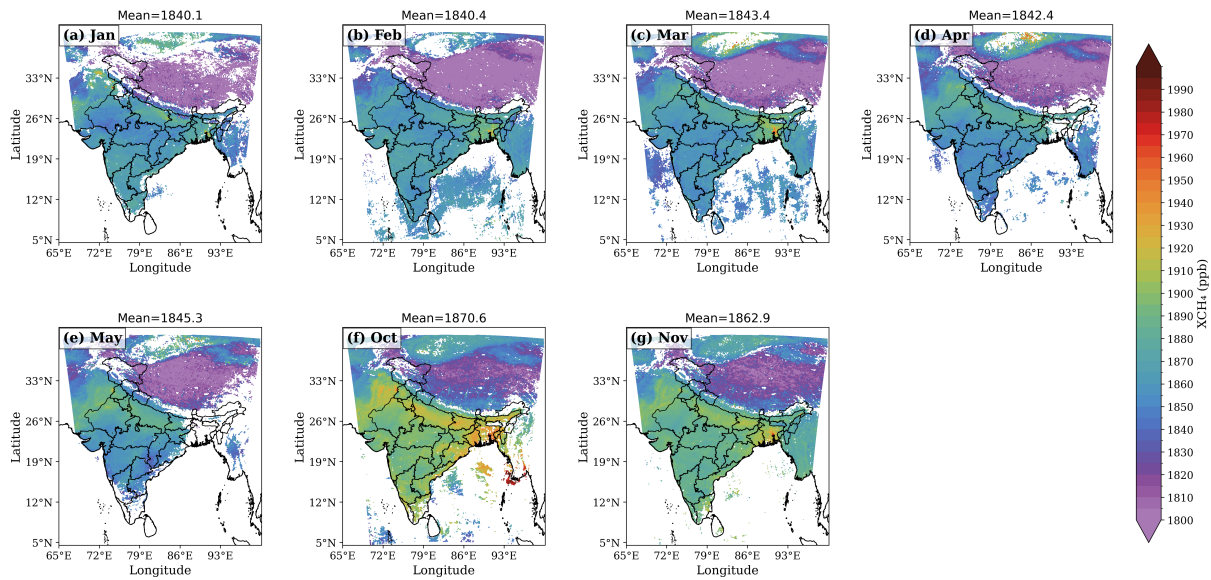


**Figure 7.** Spatial distribution of the TROPOMI Sentinel-5P measurements, averaged for (a)-(g) each available month in 2018. Some months are excluded due to insufficient data points, due to filtering using the quality flag as given in the data product.

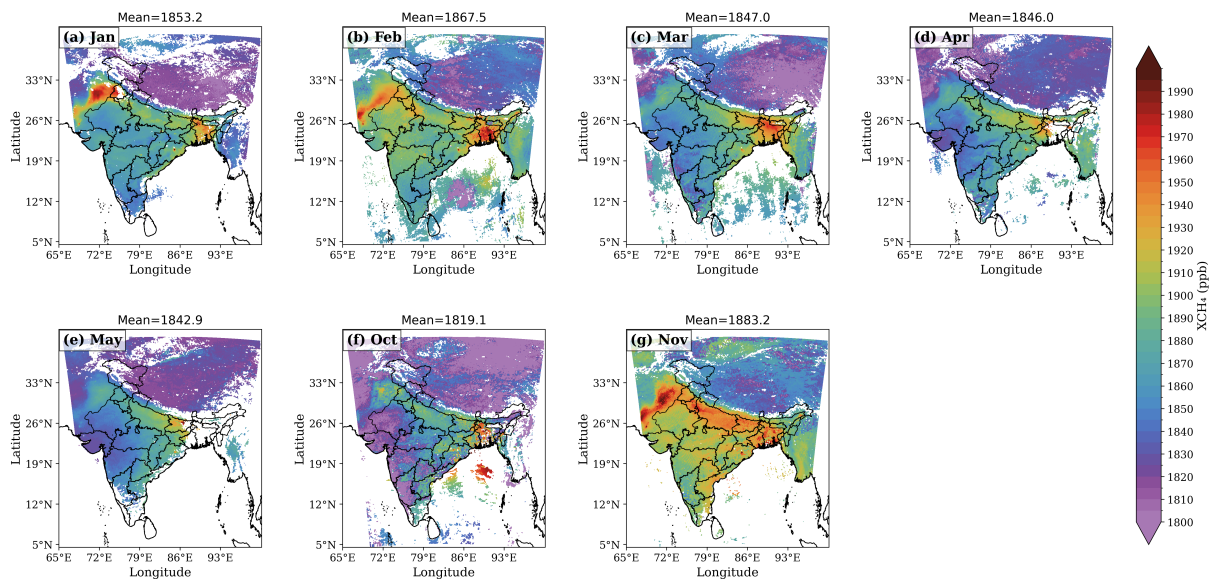


**Figure 8.** Same as Fig. 7, but showing WRF-GHG simulations of total XCH<sub>4</sub>

filtering are provided in Schneising et al. (2023). TROPOMI observations show distinct seasonal variations in the large spatial domain (Fig. 7), possibly resulting from both atmospheric transport and surface emissions variations. Observations indicate highest values in the mean spatial distribution of XCH<sub>4</sub> from October to November within the range of  $\sim 1862$  to  $1870$  ppb.

365 These seasonal increments can be attributed to the combination of surface emissions, boundary layer height, and horizontal transport, which accumulates the effect of the distribution of tracers at lower atmospheric levels. These increased regional emissions, especially from anthropogenic sources, are also seen in Fig. S3 & Fig. 3, which are typical for some parts of India, like the SI and IGP, during the October-November season. However, we cannot neglect the likelihood of bias in the observations due to high aerosol loads, which impacts XCH<sub>4</sub> retrievals (Lorente et al., 2021; Hu et al., 2018; Pandey et al., 2019). All the  
370 months show significantly higher total XCH<sub>4</sub> mixing ratios over the IGP region in comparison with the other regions over India. The IGP region is more prone to biomass burning in October and November, causing more aerosols in the region. We have examined the particulate matter (PM<sub>2.5</sub>) content using the MERRA database, which indicates a heavier aerosol content due to burning during the winter, not always necessarily peaking in October but during the December-February season (Figure not shown). There is a gradual increase in XCH<sub>4</sub> mixing ratios beginning from the winter month of January till March, with a  
375 slight dip in April and then a distinctly high increment in October (exceeding 1870 ppb) in October over the IGP (see Fig. 7. (a)-(f)).

We find that the WRF simulations generally overestimate the total XCH<sub>4</sub> mixing ratio over the Indian region compared to TROPOMI observations, peaking in winter months (maximum at 1883 ppb; see Fig. 8). The IGP emission hotspot is also pronounced in the EDGAR inventory (Fig. S2, see Sect. 4.1), suggesting the large impact of anthropogenic emissions on the  
380 observed total XCH<sub>4</sub>. Further, the sectoral analysis of the EDGAR emission inventory and the consistency of the spatial pattern with TROPOMI observations indicate that the enhancement over the IGP hotspot can be attributed to anthropogenic emissions from the large cattle population and agricultural activities, especially rice production. Similarly, high XCH<sub>4</sub> values observed along the eastern coast during October and November can be attributed to the agricultural soil emissions, as seen in Fig. S2c. Wetland emissions also peak on the eastern coast, but the emissions are not found to be high enough to affect the mixing ratio  
385 enhancement significantly (see Fig. S10 & S12). Table S1 shows the mean observed XCH<sub>4</sub> and the variability over the entire study domain for the non-monsoon months of 2018 and 2019.

In general, the WRF-GHG simulations tend to show high bias in the winter months (see Fig. 9). A definite and widespread underestimation by the model was found in October 2018. However, in 2019, WRF-GHG was almost able to capture the observed XCH<sub>4</sub>. In the summer months, the model shows patterns of overestimation in eastern India and underestimation in  
390 western India. These regional differences in patterns of XCH<sub>4</sub> can arise from heterogeneous sectorial distributions of surface emissions with seasonality that would have been misrepresented in the inventories in conjunction with the large-scale meteorological influences (e.g. southwest monsoon over India, Chandra et al. (2017)).

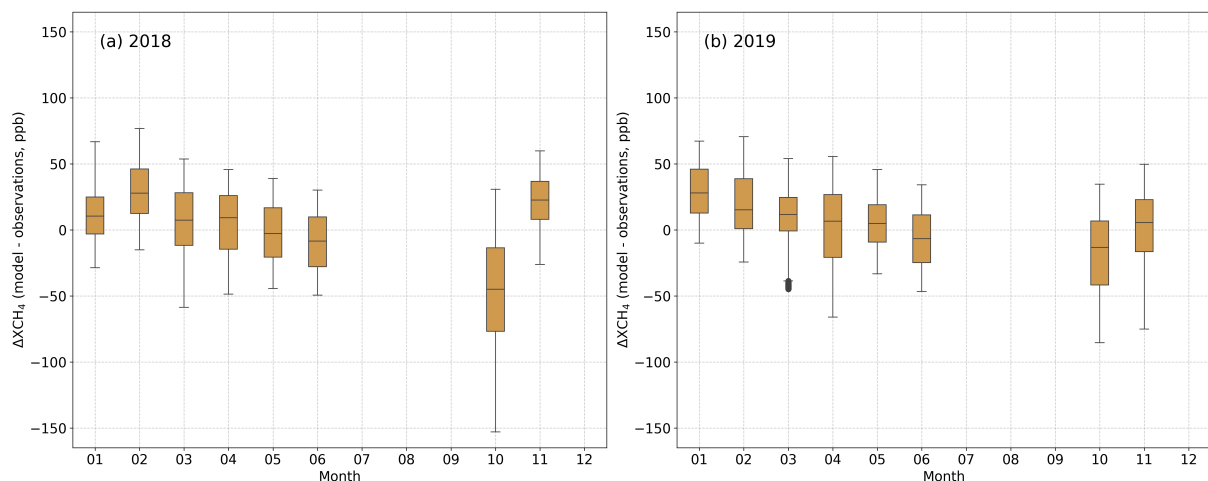


**Figure 9.** Monthly distribution of the difference between WRF-GHG simulations and TROPOMI Sentinel-5p retrievals of XCH<sub>4</sub> for each available month in 2018 and 2019 when sufficient observations are available (Outliers are not removed; instead, a 90 % winsorization (Wilcox, 2005) is applied for the outliers.)

While the peak total column XCH<sub>4</sub> for TROPOMI falls in October (~ 1870 ppb), that of the WRF-GHG simulations is in November (~ 1883 ppb). However, it is noteworthy that both the model and observation indicate the XCH<sub>4</sub> peak in either of the winter months between October and February. The WRF-GHG simulations show a higher variability (standard deviation) than observations for each month. WRF-GHG overestimates the XCH<sub>4</sub> values with a bias of ~13 (29) ppb in 2018 (2019)(see Table S1).

### 3.5 National CH<sub>4</sub> budget estimation via inverse optimization

In this section, we present estimates of India's anthropogenic CH<sub>4</sub> budget for the period 2018-2019, derived through inverse optimization as described in Sect. 3.2. We report posterior emissions separately: one with the impact of biomass burning included and another with biomass burning excluded. The EDGAR emission inventory reports an annual mean CH<sub>4</sub> emission budget of 28.7 Tg yr<sup>-1</sup>, and we assumed 80% uncertainty (23 Tg yr<sup>-1</sup>) in our prior as discussed in section 3.1. The posterior annual emission estimate is 24.3 Tg, with the uncertainty reduced to 3.3 Tg. The percentage of error reduction (calculated using Eq. 8) for monthly posterior fluxes ranges from 68 to 92 %. Our inverse model results indicate an overestimation of 14 to 23 % in the EDGAR inventory. Incorporating biomass burning emissions from GFAS has an impact of +0.3 Tg yr<sup>-1</sup> on both prior and posterior emission estimates over the Indian region. Although we focus on the national inversion estimates, owing to the inversion approach incorporated, a regional analysis (consistent with Sect. 3.1) of prior and posterior estimates has been presented in Fig. S13 and Fig. S14. As explained in Sect. 2.4.1, we examined the impact of differences in the retrieval

algorithm (see Fig. S1), considering the worst-case scenario, on annual posterior flux estimates for the year 2018, showing  
410 that the posterior uncertainty increased to 4.4 Tg yr<sup>-1</sup> from 3.5 Tg yr<sup>-1</sup> at the national scale. Future research is required for  
fully characterizing the impact of retrieval error uncertainty on posterior flux estimations at a fine scale by employing a more  
advanced inverse configuration that incorporates higher state space discretization and a detailed sensitivity analysis.

As per the India Fourth Biennial Update Report (BUR4) submitted to the United Nations Framework Convention on Climate  
Change (UNFCCC) (MoEFCC, 2024), the CH<sub>4</sub> emission budget for India is approximately 19.6 Tg yr<sup>-1</sup>, which is around 32  
415 % less than the EDGAR-reported emissions during the 2018-2019 period. Previous studies also reported an overestimation of  
the global emission inventories over India. For instance, Qu et al. (2021) report 41–57 Tg yr<sup>-1</sup> anthropogenic CH<sub>4</sub> emission  
from India, which is significantly higher than our estimations. Also, Zhang et al. (2021) estimate Indian anthropogenic methane  
emissions of 33±0.6 Tg yr<sup>-1</sup>, higher than this study estimates. However, the Global Methane Budget (2000-2017, Saunio et al.  
(2019)), based on top-down approaches using in-situ and GOSAT observations, suggest 25 Tg yr<sup>-1</sup> of anthropogenic CH<sub>4</sub> emis-  
420 sion from India, but acknowledging large uncertainty ranges in their estimations. Also, bottom-up models' estimates that are  
compiled in Saunio et al. (2019) and Jackson et al. (2020) indicate a mean anthropogenic CH<sub>4</sub> emission of 21-24 Tg yr<sup>-1</sup> from  
India. The above two estimates align with our results, though we used independent observations and a different modeling ap-  
proach. The recent updates on the Global Methane Budget (2000-2020, Saunio et al. (2025)) indicate anthropogenic methane  
emissions of 37-49 Tg yr<sup>-1</sup> for South Asia (including Afghanistan, Bangladesh, Bhutan, India, Nepal, Pakistan, and Sri Lanka),  
425 in which around 21.7 Tg yr<sup>-1</sup> are contributed from the Indian region (calculated using the data prescribed from Martinez et al.  
(2024)). Janardanan et al. (2024) reported the annual averaged (2009 - 2020) CH<sub>4</sub> emissions from anthropogenic sectors over  
the India as 24.2 ± 2.1 Tg yr<sup>-1</sup> which is close to our results. The total CH<sub>4</sub> emissions derived from a combination of satellite  
data (GOSAT), surface and aircraft measurements, and the atmospheric transport model for 2010–2015 were found to be 22  
Tg yr<sup>-1</sup>, which is substantially lower than the emissions reported by the EDGAR v4.2 inventory (Ganesan et al., 2017). On  
430 the other hand, Raju et al. (2022) reported that the CH<sub>4</sub> budget for peninsular India is 0.13 Tg yr<sup>-1</sup> higher than EDGAR v6.0  
inventory-based estimates for the period 2017-2018. These variations in emission reports emphasize the need to improve CH<sub>4</sub>  
emission estimation in India using more regional-specific information and robust methodologies. Our findings also highlight  
that top-down evaluations of emissions inventories are critical for implementing effective climate change mitigation strategies  
for countries like India that are largely understudied and undersampled, leading to poor quantification of their contributions in  
435 the context of global climate policies.

Although we utilize high-density, high-quality, and high-resolution TROPOMI satellite retrievals together with a high-  
resolution transport model, our inversion algorithm is limited by its dependence on the spatial distribution of emissions in

prior inventories. Our optimization adjusts the magnitude of prior emissions over the target region by utilizing additional information from independent measurements, but the present inverse modeling design has the limitation to minimize any flux errors in the sub-scale spatial distribution. However, we expect that those spatial errors may have a minor impact on our annual national estimates owing to our temporal and spatial averaging. We excluded natural wetland emissions from the inverse optimization as they have resulted in negligible impacts on the column mixing ratio enhancement (Fig. S10), which is smaller than the uncertainty of the satellite measurement. However, Indian wetland emissions also vary among bottom-up inventories and prior models. Approximately 7.5 Tg wetland CH<sub>4</sub> emissions from the Indian region were reported in the Global Methane Budget 2000-2020 (Saunois et al., 2024). Janardanan et al. (2024) used wetland prior emissions from the Global Methane Budget 2000-2017 (Saunois et al., 2019) in their inversions and reported approximately  $3.8 \pm 0.16$  Tg CH<sub>4</sub> emissions annually from Indian wetlands. At the same time, the BUR4 report (MoEFCC, 2024) has not included the wetland emission estimates, possibly due to inadequate data coverage. Bernard et al. (2025) also discussed the limitations in modeling the wetland emissions from the tropical region due to the inadequacy of available measurements. The above level of estimation discrepancies calls for a country-specific wetland inventory that can also be used as reliable prior fluxes in future inverse modeling. Also, there could be a possible overlapping of natural and anthropogenic (agricultural fields) wetlands in the emission inventories used, which may overestimate the sectoral contribution of posterior fluxes (Zhang et al., 2014). Another limitation could be that though the GFAS inventory includes agricultural residue burning, small fires that are common in smallholders for clearing the wastes and field preparation can be missed from prior inventories, as reported in Deshpande et al. (2022). Also, in this study, our focus is restricted to providing national-scale anthropogenic CH<sub>4</sub> emission estimates. While the inversion framework in principle allows for analysis at finer spatial or sectoral scales, here we intentionally report only the aggregated national totals, as our aim is to evaluate the feasibility of TROPOMI–WRF-GHG for constraining India’s methane budget. A more detailed exploration of sectoral and regional signals is left to future work with more coverage of observations and the implementation of more advanced inverse modeling methods.

## 460 4 Conclusions

In this study, we investigate the potential of TROPOMI satellite observations along with a high-resolution atmospheric transport model, WRF-GHG, to represent the distribution of CH<sub>4</sub> emissions over the Indian region. Analysis of the bottom-up inventories shows enteric fermentation as the most significant contributor to CH<sub>4</sub> emissions in India (42.9 %), followed by wastewater treatment (19.2 %), agricultural soil (12.4 %), fuel exploitation (6.7 %), and wetlands (5.2 %, excluding agriculture). The above proportions highlight the considerable impact of anthropogenic sources on CH<sub>4</sub> accumulation in the atmosphere. As expected,

CH<sub>4</sub> emissions from rice agriculture (August), wetlands (July), and biomass burning (March) exhibit distinct seasonal patterns. The bottom-up anthropogenic CH<sub>4</sub> emissions, and consequently the total atmospheric XCH<sub>4</sub> mixing ratios, have shown some peaks over South India due to a few prominent emission hotspots. This study characterizes regional and seasonal methane-emission patterns from global bottom-up inventories and assesses their possible influence on XCH<sub>4</sub> enhancements. The analysis  
470 identifies key uncertainty drivers such as the elevated anthropogenic emissions in the post-monsoon months, thereby guiding refinement of top-down CH<sub>4</sub> estimates across India.

The WRF-GHG simulations of XCH<sub>4</sub> mixing ratio enhancements indicate considerable contributions from anthropogenic and biomass burning emissions, particularly in the IGP region (from 27 to 67 ppb). The highest seasonal enhancements of anthropogenic XCH<sub>4</sub> occur during winter, influenced by agricultural emissions, biomass burning, and atmospheric winter  
475 transport. This inference aligns with previous studies (eg. Patra et al. (2011)) that shows stronger vertical mixing during the summer, associated with higher boundary layers and faster wind speeds, may impact CH<sub>4</sub> columns. Both the observed and modeled total XCH<sub>4</sub> show significant peaks over the IGP region, with values ranging from ~1862 to ~1870 ppb during October-November. Though WRF-GHG remarkably captures atmospheric XCH<sub>4</sub> patterns, simulations generally overestimate XCH<sub>4</sub> levels compared to TROPOMI. The total XCH<sub>4</sub> along the eastern coast reflects the influence of agricultural soil emissions on  
480 column-averaged methane. Although wetland emissions peak in this region, their contribution to atmospheric mixing ratios is negligible. Our high-resolution model is capable of capturing surface CH<sub>4</sub> variability, especially for the well-mixed conditions, as confirmed by the ground-based CH<sub>4</sub> observations. However, this comparison is representative of only one station, though it is a complicated measurement location to be represented by the model owing to the influence of coastal meteorology. Such ground-based observations across India are essential for evaluating the full potential of high-resolution models in representing  
485 the atmospheric distribution of trace gases and to better constrain vertical transport processes and regional representativeness.

The inversion analysis using our high-resolution model and TROPOMI observations reports an annual mean anthropogenic CH<sub>4</sub> emission budget of  $24.3 \pm 3.3 \text{ Tg yr}^{-1}$  (excluding biomass burning of  $0.3 \text{ Tg yr}^{-1}$ ). Our estimations are 14 to 23 % lower than the EDGAR emission estimates. At the same time, our estimate is 19 % higher than what the Government of India reported to the UNFCCC for the same period but close to the latest Global Methane Budget 2000-2020. We emphasize the  
490 need for a robust reporting of CH<sub>4</sub> emissions from the Indian region in the global emission inventories, which also require more ground-based atmospheric trace gas measurements along with the advancement of satellite capabilities and atmospheric tracer transport models. With the advancements of denser observational coverage and the high-quality atmospheric transport models, future research can thus explore and evaluate different inverse techniques like ensemble Kalman filter (EnKF) and 4D variational inversion (4D-Var) that can handle highly resolved state vectors, leading to improved emissions at a much finer

495 sub-scale. Overall, the analyses highlight that TROPOMI observations can offer valuable insights into CH<sub>4</sub> emissions, and the WRF-GHG model has the potential to be used in the assimilation system to refine the emissions.

*Code and data availability.* The anthropogenic CH<sub>4</sub> emission inventories used in this study are downloaded from [https://edgar.jrc.ec.europa.eu/archived\\_datasets](https://edgar.jrc.ec.europa.eu/archived_datasets) (last access: March 2024) (Crippa et al., 2024). CAMS global biomass burning emission based on fire radiative power (GFAS) is accessed from Copernicus Atmosphere Monitoring Service (CAMS) Atmosphere Data Store, DOI: 10.24381/a05253c7 (last  
500 access : November 2023). The global wetland CH<sub>4</sub> emissions, WetCHARTs v1.3.1 is prescribed from <https://daac.ornl.gov/cgi-bin/> (last access: November 2023) (Bloom et al., 2017). The WRF source code is freely available and can be accessed from [https://www2.mmm.ucar.edu/wrf/users/download/get\\_source.html](https://www2.mmm.ucar.edu/wrf/users/download/get_source.html). The TROPOMI/WFMD v1.8 product is made available via [https://www.iup.uni-bremen.de/carbon\\_ghg/products/tropomi\\_wfmd/](https://www.iup.uni-bremen.de/carbon_ghg/products/tropomi_wfmd/).

*Author contributions.* DP designed the study, TAM and DP performed the model simulations, raw data analysis, and postprocessing, and  
505 wrote the initial version of the manuscript. JS, MVD, VT, and AR contributed to the data curation and figures. MB and OS contributed to data archival and processing. SBK contributed to editing. SS, IAG, and SB contributed to the ground-based data collection and pre-processing. All authors contributed to the data analysis, interpretation and writing.

*Competing interests.* The corresponding author has declared that none of the authors has any competing interests.

*Disclaimer.* Publisher's note: Copernicus Publications remains neutral with regard to jurisdictional claims made in the text, published maps,  
510 institutional affiliations, or any other geographical representation in this paper. While Copernicus Publications makes every effort to include appropriate place names, the final responsibility lies with the authors.

*Acknowledgements.* This study has been supported by funding from the Indian Ministry of Education and the Max Planck Society in Germany, which has been allocated to IISERB. The University of Bremen team acknowledges funding from ESA via project GHG-CCI+ (ESA contract no. 4000126450/19/I-NB) and the Bundesministerium für Bildung und Forschung within its project ITMS (grant no. 01  
515 LK2103A). We acknowledge the support of IISERB's high-performance cluster system for computations, data analysis, and visualization.

The TROPOMI/WFMD retrievals were performed on HPC facilities funded by the Deutsche Forschungsgemeinschaft (grant nos. INST 144/379-1 FUGG and INST 144/493-1 FUGG). This publication contains modified Copernicus Sentinel data (2018–2019). Sentinel-5 Precursor is an ESA mission implemented on behalf of the European Commission. The TROPOMI payload is a joint development by ESA and the Netherlands Space Office (NSO). The Sentinel-5 Precursor ground segment development has been funded by ESA and with national contributions from the Netherlands, Germany, and Belgium. Thara Anna Mathew acknowledges the financial support provided by the Prime Minister's Research Fellowship (PMRF) Scheme for providing a fellowship for a PhD. Jithin Sukumaran acknowledges the Council of Scientific and Industrial Research (CSIR) funding for his PhD fellowship. Imran A Girach acknowledges Prabha R Nair, former scientist at SPL, for supporting the surface trace gas measurements at Thumba utilized in this study. Special thanks to Navaneetha Jayan and Advait J Vinod for their help with the graphics.

## 525 **References**

- Agarwal, R. and Garg, J.: Methane emission modelling from wetlands and waterlogged areas using MODIS data, *Current Science*, pp. 36–40, 2009.
- Agustí-Panareda, A., Barré, J., Massart, S., Inness, A., Aben, I., Ades, M., Baier, B. C., Balsamo, G., Borsdorff, T., Bousserez, N., Boussetta, S., Buchwitz, M., Cantarello, L., Crevoisier, C., Engelen, R., Eskes, H., Flemming, J., Garrigues, S., Hasekamp, O., Huijnen, V., Jones, L., Kipling, Z., Langerock, B., McNorton, J., Meilhac, N., Noël, S., Parrington, M., Peuch, V.-H., Ramonet, M., Razinger, M., Reuter, M., Ribas, R., Suttie, M., Sweeney, C., Tarniewicz, J., and Wu, L.: Technical note: The CAMS greenhouse gas reanalysis from 2003 to 2020, *Atmospheric Chemistry and Physics*, 23, 3829–3859, <https://doi.org/10.5194/acp-23-3829-2023>, 2023.
- Agustí-Panareda, A., Barré, J., Massart, S., Inness, A., Aben, I., Ades, M., Baier, B. C., Balsamo, G., Borsdorff, T., Bousserez, N., et al.: The CAMS greenhouse gas reanalysis from 2003 to 2020, *Atmospheric Chemistry and Physics*, 23, 3829–3859, <https://doi.org/10.5194/acp-23-3829-2023>, 2023.
- Alexe, M., Bergamaschi, P., Segers, A., Detmers, R., Butz, A., Hasekamp, O., Guerlet, S., Parker, R., Boesch, H., Frankenberg, C., et al.: Inverse modelling of CH<sub>4</sub> emissions for 2010–2011 using different satellite retrieval products from GOSAT and SCIAMACHY, *Atmospheric Chemistry and Physics*, 15, 113–133, <https://doi.org/10.5194/acp-15-113-2015>, 2015.
- Anand, S., Dahiya, R., Talyan, V., and Vrat, P.: Investigations of methane emissions from rice cultivation in Indian context, *Environment International*, 31, 469–482, <https://doi.org/10.1016/j.envint.2004.10.016>, 2005.
- Baer, D. S., Paul, J. B., Gupta, M., and O’keefe, A.: Sensitive absorption measurements in the near-infrared region using off-axis integrated-cavity-output spectroscopy, *Applied Physics B*, 75, 261–265, <https://doi.org/10.1007/s00340-002-0971-z>, 2002.
- Beck, V.: The WRF Greenhouse Gas Model (WRF-GHG), 2011.
- Bergamaschi, P., Karstens, U., Manning, A. J., Saunois, M., Tsuruta, A., Berchet, A., Vermeulen, A. T., Arnold, T., Janssens-Maenhout, G., Hammer, S., et al.: Inverse modelling of European CH<sub>4</sub> emissions during 2006–2012 using different inverse models and reassessed atmospheric observations, *Atmospheric Chemistry and Physics*, 18, 901–920, <https://doi.org/10.5194/acp-18-901-2018>, 2018.
- Bernard, J., Salmon, E., Saunois, M., Peng, S., Serrano-Ortiz, P., Berchet, A., Gnanamoorthy, P., Jansen, J., and Ciais, P.: Satellite-based modeling of wetland methane emissions on a global scale (SatWetCH<sub>4</sub> 1.0), *Geoscientific Model Development*, 18, 863–883, <https://doi.org/10.5194/egusphere-2024-1331>, 2025.
- Bloom, A., Bowman, K., Lee, M., Turner, A., Schroeder, R., Worden, J., Weidner, R., McDonald, K., and Jacob, D.: CMS: global 0.5-deg wetland methane emissions and uncertainty (WetCHARTs v1. 3.1), ORNL DAAC, <https://doi.org/10.3334/ORNLDAAC/1915>, 2021.
- Bloom, A. A., Bowman, K. W., Lee, M., Turner, A. J., Schroeder, R., Worden, J. R., Weidner, R., McDonald, K. C., and Jacob, D. J.: A global wetland methane emissions and uncertainty dataset for atmospheric chemical transport models (WetCHARTs version 1.0), *Geoscientific Model Development*, 10, 2141–2156, <https://doi.org/10.5194/gmd-10-2141-2017>, 2017.

- 555 Buchwitz, M., Khlystova, I., Bovensmann, H., and Burrows, J.: Three years of global carbon monoxide from SCIAMACHY: comparison with MOPITT and first results related to the detection of enhanced CO over cities, *Atmospheric Chemistry and Physics*, 7, 2399–2411, <https://doi.org/10.5194/acp-7-2399-2007>, 2007.
- Buchwitz, M., Schneising, O., Reuter, M., Heymann, J., Krautwurst, S., Bovensmann, H., Burrows, J. P., Boesch, H., Parker, R. J., Somkuti, P., et al.: Satellite-derived methane hotspot emission estimates using a fast data-driven method, *Atmospheric Chemistry and Physics*, 17, 5751–5774, <https://doi.org/10.5194/acp-17-5751-2017>, 2017.
- 560 Buchwitz, M. d., De Beek, R., Burrows, J., Bovensmann, H., Warneke, T., Notholt, J., Meirink, J., Goede, A., Bergamaschi, P., Körner, S., et al.: Atmospheric methane and carbon dioxide from SCIAMACHY satellite data: initial comparison with chemistry and transport models, *Atmospheric Chemistry and Physics*, 5, 941–962, <https://doi.org/10.5194/acp-5-941-2005>, 2005.
- Butz, A., Guerlet, S., Hasekamp, O., Schepers, D., Galli, A., Aben, I., Frankenberg, C., Hartmann, J.-M., Tran, H., Kuze, A., et al.: Toward accurate CO<sub>2</sub> and CH<sub>4</sub> observations from GOSAT, *Geophysical Research Letters*, 38, <https://doi.org/10.1029/2011GL047888>, 2011.
- 565 Chandra, N., Hayashida, S., Saeki, T., and Patra, P. K.: What controls the seasonal cycle of columnar methane observed by GOSAT over different regions in India?, *Atmospheric Chemistry and Physics*, 17, 12 633–12 643, <https://doi.org/10.5194/acp-17-12633-2017>, 2017.
- Chen, Z., Jacob, D. J., Nesser, H., Sulprizio, M. P., Lorente, A., Varon, D. J., Lu, X., Shen, L., Qu, Z., Penn, E., et al.: Methane emissions from China: a high-resolution inversion of TROPOMI satellite observations, *Atmospheric Chemistry and Physics*, 22, 10 809–10 826, <https://doi.org/10.5194/acp-22-10809-2022>, 2022.
- 570 Crippa, M., Solazzo, E., Huang, G., Guizzardi, D., Koffi, E., Muntean, M., Schieberle, C., Friedrich, R., and Janssens-Maenhout, G.: High resolution temporal profiles in the Emissions Database for Global Atmospheric Research, *Scientific data*, 7, 121, <https://doi.org/10.6084/m9.figshare.12052887>, 2020.
- Crippa, M., Guizzardi, D., Pagani, F., Schiavina, M., Melchiorri, M., Pisoni, E., Graziosi, F., Muntean, M., Maes, J., Dijkstra, L., et al.: Insights on the spatial distribution of global, national and sub-national GHG emissions in edgarv8. 0, *Earth System Science Data Discussions*, 2023, 1–28, <https://doi.org/10.5194/essd-16-2811-2024>, 2023.
- 575 Crippa, M., Guizzardi, D., Pagani, F., Schiavina, M., Melchiorri, M., Pisoni, E., Graziosi, F., Muntean, M., Maes, J., Dijkstra, L., et al.: Insights into the spatial distribution of global, national, and subnational greenhouse gas emissions in the Emissions Database for Global Atmospheric Research (EDGAR v8. 0), *Earth System Science Data*, 16, 2811–2830, <https://doi.org/10.5194/essd-16-2811-2024>, 2024.
- 580 Cusworth, D. H., Jacob, D. J., Sheng, J.-X., Benmergui, J., Turner, A. J., Brandman, J., White, L., and Randles, C. A.: Detecting high-emitting methane sources in oil/gas fields using satellite observations, *Atmospheric Chemistry and Physics*, 18, 16 885–16 896, <https://doi.org/10.5194/acp-18-16885-2018>, 2018.
- Das, N., Chakraborty, R., Pal, S. C., Mondal, A., and Mandal, S.: A novel coupled framework for detecting hotspots of methane emission from the vulnerable Indian Sundarban mangrove ecosystem using data-driven models, *Science of The Total Environment*, 866, 161 319, <https://doi.org/10.1016/j.scitotenv.2022.161319>, 2023.
- 585

- de Gouw, J., Veefkind, J., Roosenbrand, E., Dix, B., Lin, J., Landgraf, J., and Levelt, P.: Daily Satellite Observations of Methane from Oil and Gas Production Regions in the United States, *Scientific Reports*, 10, <https://doi.org/10.1038/s41598-020-57678-4>, 2020.
- Deshpande, M. V., Pillai, D., and Jain, M.: Detecting and quantifying residue burning in smallholder systems: An integrated approach using Sentinel-2 data, *International Journal of Applied Earth Observation and Geoinformation*, 108, 102761, <https://doi.org/10.1016/j.jag.2022.102761>, 2022.
- 590 Eskes, H. and Boersma, K.: Averaging kernels for DOAS total-column satellite retrievals, *Atmospheric Chemistry and Physics*, 3, 1285–1291, <https://doi.org/10.5194/acp-3-1285-2003>, 2003.
- Friedlingstein, P., O’sullivan, M., Jones, M. W., Andrew, R. M., Hauck, J., Landschützer, P., Le Quéré, C., Li, H., Luijkx, I. T., Olsen, A., et al.: Global carbon budget 2024, *Earth System Science Data Discussions*, 2024, 1–133, 2024.
- 595 Ganesan, A. L., Rigby, M., Lunt, M. F., Parker, R. J., Boesch, H., Goulding, N., Umezawa, T., Zahn, A., Chatterjee, A., Prinn, R. G., et al.: Atmospheric observations show accurate reporting and little growth in India’s methane emissions, *Nature Communications*, 8, 836, <https://doi.org/DOI: 10.1038/s41467-017-00994-7>, 2017.
- Garg, A., Kankal, B., and Shukla, P.: Methane emissions in India: Sub-regional and sectoral trends, *Atmospheric environment*, 45, 4922–4929, <https://doi.org/10.1016/j.atmosenv.2011.06.004>, 2011.
- 600 Guha, T., Tiwari, Y. K., Valsala, V., Lin, X., Ramonet, M., Mahajan, A., Datye, A., and Kumar, K. R.: What controls the atmospheric methane seasonal variability over India?, *Atmospheric Environment*, 175, 83–91, <https://doi.org/10.1016/j.atmosenv.2017.11.042>, 2018.
- Gururaj Katti, G. K., Pasalu, I., Rao, P., Varma, N., and Krishnaiah, K.: Farmer’s participatory approach to improve pest management decision making in high production systems of rice in Andhra Pradesh-a case study., <https://doi.org/DOI: 10.1080/14735903.2022.2070340>, 2002.
- 605 Heald, C. L., Jacob, D. J., Jones, D. B., Palmer, P. I., Logan, J. A., Streets, D., Sachse, G. W., Gille, J. C., Hoffman, R. N., and Nehr Korn, T.: Comparative inverse analysis of satellite (MOPITT) and aircraft (TRACE-P) observations to estimate Asian sources of carbon monoxide, *Journal of Geophysical Research: Atmospheres*, 109, <https://doi.org/10.1029/2004JD005185>, 2004.
- Hersbach, H., Bell, B., Berrisford, P., Hirahara, S., Horányi, A., Muñoz-Sabater, J., Nicolas, J., Peubey, C., Radu, R., Schepers, D., et al.: The ERA5 global reanalysis, *Quarterly Journal of the Royal Meteorological Society*, 146, 1999–2049, <https://doi.org/10.1002/qj.3803>, 2020.
- Hu, H., Landgraf, J., Detmers, R., Borsdorff, T., Aan de Brugh, J., Aben, I., Butz, A., and Hasekamp, O.: Toward global mapping of methane with TROPOMI: First results and intersatellite comparison to GOSAT, *Geophysical Research Letters*, 45, 3682–3689, <https://doi.org/10.1002/2018GL077259>, 2018.
- Inness, A., Ades, M., Agustí-Panareda, A., Barré, J., Benedictow, A., Blechschmidt, A.-M., Dominguez, J. J., Engelen, R., Eskes, H., Fleming, J., et al.: The CAMS reanalysis of atmospheric composition, *Atmospheric Chemistry and Physics*, 19, 3515–3556, 2019.
- Jackson, R. B., Saunio, M., Bousquet, P., Canadell, J. G., Poulter, B., Stavert, A. R., Bergamaschi, P., Niwa, Y., Segers, A., and Tsuruta, A.: 615 Increasing anthropogenic methane emissions arise equally from agricultural and fossil fuel sources, *Environmental Research Letters*, 15, 071 002, <https://doi.org/10.1088/1748-9326/ab9ed2>, 2020.

- Jacob, D. J., Turner, A. J., Maasackers, J. D., Sheng, J., Sun, K., Liu, X., Chance, K., Aben, I., McKeever, J., and Frankenberg, C.: Satellite observations of atmospheric methane and their value for quantifying methane emissions, *Atmospheric Chemistry and Physics*, 16, 14 371–14 396, <https://doi.org/10.5194/acp-16-14371-2016>, 2016.
- 620 Jacob, D. J., Varon, D. J., Cusworth, D. H., Dennison, P. E., Frankenberg, C., Gautam, R., Guanter, L., Kelley, J., McKeever, J., Ott, L. E., et al.: Quantifying methane emissions from the global scale down to point sources using satellite observations of atmospheric methane, *Atmospheric Chemistry and Physics*, 22, 9617–9646, <https://doi.org/10.5194/acp-22-9617-2022>, 2022.
- Janardanan, R., Maksyutov, S., Wang, F., Nayagam, L., Sahu, S. K., Mangaraj, P., Saunio, M., Lan, X., and Matsunaga, T.: Country-level methane emissions and their sectoral trends during 2009–2020 estimated by high-resolution inversion of GOSAT and surface observations, *Environmental Research Letters*, 19, 034 007, <https://doi.org/DOI 10.1088/1748-9326/ad2436>, 2024.
- 625 Janssens-Maenhout, G., Crippa, M., Guizzardi, D., Muntean, M., and Schaaf, E.: Emissions Database for Global Atmospheric Research (EDGAR), version v4.2 (time-series), <http://data.europa.eu/89h/jrc-edgar-emissiontimeseriesv42>, 2011.
- Kaiser, J., Heil, A., Andreae, M., Benedetti, A., Chubarova, N., Jones, L., Morcrette, J.-J., Razinger, M., Schultz, M., Suttie, M., et al.: Biomass burning emissions estimated with a global fire assimilation system based on observed fire radiative power, *Biogeosciences*, 9, 527–554, <https://doi.org/10.5194/bg-9-527-2012>, 2012.
- 630 Kavitha, M., Nair, P. R., Girach, I., Aneesh, S., Sijikumar, S., and Renju, R.: Diurnal and seasonal variations in surface methane at a tropical coastal station: Role of mesoscale meteorology, *Science of The Total Environment*, 631–632, 1472–1485, <https://doi.org/10.1016/j.scitotenv.2018.03.123>, 2018.
- Kretschmer, R., Gerbig, C., Karstens, U., Biavati, G., Vermeulen, A., Vogel, F., Hammer, S., and Totsche, K.: Impact of optimized mixing heights on simulated regional atmospheric transport of CO<sub>2</sub>, *Atmospheric Chemistry and Physics*, 14, 7149–7172, <https://doi.org/10.5194/acp-14-7149-2014>, 2014.
- 635 Lee, H., Calvin, K., Dasgupta, D., Krinner, G., Mukherji, A., Thorne, P., Trisos, C., Romero, J., Aldunce, P., Barret, K., et al.: IPCC, 2023: Climate Change 2023: Synthesis Report, Summary for Policymakers. Contribution of Working Groups I, II and III to the Sixth Assessment Report of the Intergovernmental Panel on Climate Change [Core Writing Team, H. Lee and J. Romero (eds.)]. IPCC, Geneva, Switzerland., 2023.
- 640 Liang, R., Zhang, Y., Chen, W., Zhang, P., Liu, J., Chen, C., Mao, H., Shen, G., Qu, Z., Chen, Z., et al.: East Asian methane emissions inferred from high-resolution inversions of GOSAT and TROPOMI observations: a comparative and evaluative analysis, *Atmospheric Chemistry and Physics*, 23, 8039–8057, <https://doi.org/10.5194/acp-23-8039-2023>, 2023.
- Lin, X., Indira, N., Ramonet, M., Delmotte, M., Ciais, P., Bhatt, B., Reddy, M., Angchuk, D., Balakrishnan, S., Jorphail, S., et al.: Long-lived atmospheric trace gases measurements in flask samples from three stations in India, *Atmospheric Chemistry and Physics*, 15, 9819–9849, <https://doi.org/10.5194/acp-15-9819-2015>, 2015.

- Lorente, A., Borsdorff, T., Butz, A., Hasekamp, O., Schneider, A., Wu, L., Hase, F., Kivi, R., Wunch, D., Pollard, D. F., et al.: Methane retrieved from TROPOMI: improvement of the data product and validation of the first 2 years of measurements, *Atmospheric Measurement Techniques*, 14, 665–684, <https://doi.org/10.5194/amt-14-665-2021>, 2021.
- 650 Lu, X., Jacob, D. J., Wang, H., Maasakkers, J. D., Zhang, Y., Scarpelli, T. R., Shen, L., Qu, Z., Sulprizio, M. P., Nesser, H., et al.: Methane emissions in the United States, Canada, and Mexico: evaluation of national methane emission inventories and 2010–2017 sectoral trends by inverse analysis of in situ (GLOBALVIEWplus CH 4 ObsPack) and satellite (GOSAT) atmospheric observations, *Atmospheric Chemistry and Physics*, 22, 395–418, <https://doi.org/10.5194/acp-22-395-2022>, 2022.
- Maasakkers, J. D., Jacob, D. J., Sulprizio, M. P., Scarpelli, T. R., Nesser, H., Sheng, J.-X., Zhang, Y., Hersher, M., Bloom, A. A., Bowman, 655 K. W., et al.: Global distribution of methane emissions, emission trends, and OH concentrations and trends inferred from an inversion of GOSAT satellite data for 2010–2015, *Atmospheric Chemistry and Physics*, 19, 7859–7881, <https://doi.org/10.5194/acp-19-7859-2019>, 2019.
- Madrazo, J., Clappier, A., Belalcazar, L. C., Cuesta, O., Contreras, H., and Golay, F.: Screening differences between a local inventory and the Emissions Database for Global Atmospheric Research (EDGAR), *Science of the Total Environment*, 631, 934–941, 660 <https://doi.org/10.1016/j.scitotenv.2018.03.094>, 2018.
- Manjunath, K., Panigrahy, S., Kumari, K., Adhya, T., and Parihar, J.: Spatiotemporal modelling of methane flux from the rice fields of India using remote sensing and GIS, *International Journal of Remote Sensing*, 27, 4701–4707, <https://doi.org/10.1080/01431160600702350>, 2006.
- Martinez, A., Saunio, M., Poulter, B., Bousquet, P., Canadell, J. G., Jackson, R. B., Dlugokencky, E. J., Ciais, P., Bastviken, D., Blake, 665 D. R., Castaldi, S., Etiope, G., Gedney, N., Höglund-Isaksson, L., Hugelius, G., Ito, A., Kleinen, T., Krummel, P. B., Liu, L., McDonald, K. C., Melton, J. R., Müller, J., Murguia-Flores, F., Niwa, Y., Noce, S., Parker, R. J., Peng, C., Ramonet, M., Riley, W. J., Rosentreter, J. A., Segers, A., Smith, S. J., Tian, H., Tubiello, F. N., Tsuruta, A., Weber, T. S., Werf, G. R. v. d., Worthy, D., Yoshida, Y., Zhang, W., Zhang, Z., Zheng, B., Zhu, Q., Zhu, Q., and Zhuang, Q.: Supplemental data of the Global Carbon Project methane budget 2024 v1, 2024.
- Metya, A., Datye, A., Chakraborty, S., Tiwari, Y. K., Sarma, D., Bora, A., and Gogoi, N.: Diurnal and seasonal variability of CO<sub>2</sub> and CH<sub>4</sub> 670 concentration in a semi-urban environment of western India, *Scientific reports*, 11, 2931, <https://doi.org/10.1038/s41598-021-82321-1>, 2021.
- Miller, S. M. and Michalak, A. M.: Constraining sector-specific CO<sub>2</sub> and CH<sub>4</sub> emissions in the US, *Atmospheric Chemistry and Physics*, 17, 3963–3985, <https://doi.org/10.5194/acp-17-3963-2017>, 2017.
- Miller, S. M., Michalak, A. M., Detmers, R. G., Hasekamp, O. P., Bruhwiler, L. M., and Schwietzke, S.: China’s coal mine methane regula- 675 tions have not curbed growing emissions, *Nature Communications*, 10, 303, <https://doi.org/10.1038/s41467-018-07891-7>, 2019.
- Ministry of Environment, F. and Change, C.: India: First biennial update report to the United Nations framework convention on climate change, 2015.

- MoEFCC, .: India: Fourth Biennial update report to the United Nations Framework Convention on Climate Change, Ministry of Environment, Forest and Climate Change, Government of India., 2024.
- 680 Montzka, S. A., Dlugokencky, E. J., and Butler, J. H.: Non-CO<sub>2</sub> greenhouse gases and climate change, *Nature*, 476, 43–50, <https://doi.org/doi:10.1038/nature10322>, 2011.
- Myhre, G., Myhre, C. L., Samset, B., and Storelvmo, T.: Aerosols and their relation to global climate and climate sensitivity, *Nature Education Knowledge*, 4, 7, 2013a.
- Myhre, G., Shindell, D., Bréon, F.-M., Collins, W., Fuglestedt, J., Huang, J., Koch, D., Lamarque, J.-F., Lee, D., Mendoza, B., Nakajima, T.,  
685 Rocco, A., Stephens, G., Takemura, T., and Zhang, H.: Anthropogenic and natural radiative forcing, pp. 659–740, Cambridge University Press, Cambridge, UK, <https://doi.org/10.1017/CBO9781107415324.018>, 2013b.
- Nisbet, E. G., Manning, M., Dlugokencky, E., Fisher, R., Lowry, D., Michel, S., Myhre, C. L., Platt, S. M., Allen, G., Bousquet, P., et al.: Very strong atmospheric methane growth in the 4 years 2014–2017: Implications for the Paris Agreement, *Global Biogeochemical Cycles*, 33, 318–342, <https://doi.org/10.1029/2018GB006009>, 2019.
- 690 Palmer, P. I., Feng, L., Lunt, M. F., Parker, R. J., Bösch, H., Lan, X., Lorente, A., and Borsdorff, T.: The added value of satellite observations of methane for understanding the contemporary methane budget, *Philosophical Transactions of the Royal Society A*, 379, 20210106, <https://doi.org/10.1098/rsta.2021.0106>, 2021.
- Pandey, S., Gautam, R., Houweling, S., Van Der Gon, H. D., Sadavarte, P., Borsdorff, T., Hasekamp, O., Landgraf, J., Tol, P., Van Kempen, T., et al.: Satellite observations reveal extreme methane leakage from a natural gas well blowout, *Proceedings of the National Academy of  
695 Sciences*, 116, 26376–26381, <https://doi.org/10.1073/pnas.1908712116>, 2019.
- Panigrahy, S., Upadhyay, G., Ray, S. S., and Parihar, J. S.: Mapping of cropping system for the Indo-Gangetic plain using multi-date SPOT NDVI-VGT data, *Journal of the Indian Society of Remote Sensing*, 38, 627–632, <https://doi.org/10.1007/s12524-011-0059-5>, 2010.
- Patra, P. K., Houweling, S., Krol, M., Bousquet, P., Belikov, D., Bergmann, D., Bian, H., Cameron-Smith, P., Chipperfield, M. P., Corbin, K.,  
et al.: TransCom model simulations of CH<sub>4</sub> and related species: linking transport, surface flux and chemical loss with CH<sub>4</sub> variability in  
700 the troposphere and lower stratosphere, *Atmospheric Chemistry and Physics*, 11, 12813–12837, 2011.
- Patra, P. K., Saeki, T., Dlugokencky, E. J., Ishijima, K., Umezawa, T., Ito, A., Aoki, S., Morimoto, S., Kort, E. A., Crotwell, A., et al.: Regional methane emission estimation based on observed atmospheric concentrations (2002–2012), *Journal of the Meteorological Society of Japan. Ser. II*, 94, 91–113, <https://doi.org/10.2151/jmsj.2016-006>, 2016.
- Pillai, D., Buchwitz, M., Gerbig, C., Koch, T., Reuter, M., Bovensmann, H., Marshall, J., and Burrows, J. P.: Tracking city CO<sub>2</sub> emissions  
705 from space using a high-resolution inverse modelling approach: a case study for Berlin, Germany, *Atmospheric Chemistry and Physics*, 16, 9591–9610, <https://doi.org/10.5194/acp-16-9591-2016>, 2016.
- Qu, Z., Jacob, D. J., Shen, L., Lu, X., Zhang, Y., Scarpelli, T. R., Nesser, H., Sulprizio, M. P., Maasakkers, J. D., Bloom, A. A., Worden, J. R., Parker, R. J., and Delgado, A. L.: Global distribution of methane emissions: a comparative inverse analysis of observations from

- the TROPOMI and GOSAT satellite instruments, *Atmospheric Chemistry and Physics*, 21, 14 159–14 175, <https://doi.org/10.5194/acp-21-14159-2021>, 2021.
- 710 Raju, A., Sijikumar, S., Valsala, V., Tiwari, Y. K., Halder, S., Girach, I., Jain, C. D., and Ratnam, M. V.: Regional estimation of methane emissions over the peninsular India using atmospheric inverse modelling, *Environmental Monitoring and Assessment*, 194, 647, <https://doi.org/10.1007/s10661-022-10323-1>, 2022.
- Ramasamy, C. and Manivel, S.: An analysis of aspects of performance and difficulties of poultry farming in Namakkal, Tamilnadu, 2019.
- 715 Rodgers, C. D.: Inverse methods for atmospheric sounding: theory and practice, vol. 2, World scientific, <https://doi.org/10.1142/3171>, 2000.
- Saunois, M., Bousquet, P., Poulter, B., Peregon, A., Ciais, P., Canadell, J. G., Dlugokencky, E. J., Etiope, G., Bastviken, D., Houweling, S., et al.: The global methane budget: 2000–2012, *Earth System Science Data Discussions*, 2016, 1–79, <https://doi.org/10.5194/essd-8-697-2016>, 2016.
- Saunois, M., Stavert, A. R., Poulter, B., Bousquet, P., Canadell, J. G., Jackson, R. B., Raymond, P. A., Dlugokencky, E. J., Houweling, S., Patra, P. K., et al.: The global methane budget 2000–2017, *Earth System Science Data Discussions*, 2019, 1–136, <https://doi.org/10.5194/essd-12-1561-2020>, 2019.
- 720 Saunois, M., Martinez, A., Poulter, B., Zhang, Z., Raymond, P., Regnier, P., Canadell, J. G., Jackson, R. B., Patra, P. K., Bousquet, P., et al.: Global methane budget 2000–2020, *Earth System Science Data Discussions*, 2024, 1–147, <https://doi.org/10.5194/essd-2024-115>, 2024.
- Saunois, M., Martinez, A., Poulter, B., Zhang, Z., Raymond, P. A., Regnier, P., Canadell, J. G., Jackson, R. B., Patra, P. K., Bousquet, P., Ciais, P., Dlugokencky, E. J., Lan, X., Allen, G. H., Bastviken, D., Beerling, D. J., Belikov, D. A., Blake, D. R., Castaldi, S., Crippa, M., Deemer, B. R., Dennison, F., Etiope, G., Gedney, N., Höglund-Isaksson, L., Holgerson, M. A., Hopcroft, P. O., Hugelius, G., Ito, A., Jain, A. K., Janardanan, R., Johnson, M. S., Kleinen, T., Krummel, P. B., Lauerwald, R., Li, T., Liu, X., McDonald, K. C., Melton, J. R., Mühle, J., Müller, J., Murguía-Flores, F., Niwa, Y., Noce, S., Pan, S., Parker, R. J., Peng, C., Ramonet, M., Riley, W. J., Rocher-Ros, G., Rosentreter, J. A., Sasakawa, M., Segers, A., Smith, S. J., Stanley, E. H., Thanwerdas, J., Tian, H., Tsuruta, A., Tubiello, F. N., Weber, T. S., van der Werf, G. R., Worthy, D. E. J., Xi, Y., Yoshida, Y., Zhang, W., Zheng, B., Zhu, Q., Zhu, Q., and Zhuang, Q.: Global Methane Budget 2000–2020, *Earth System Science Data*, 17, 1873–1958, <https://doi.org/10.5194/essd-17-1873-2025>, 2025.
- 725 730 Scarpelli, T. R., Roy, E., Jacob, D. J., Sulprizio, M. P., Tate, R. D., and Cusworth, D. H.: Using new geospatial data and 2020 fossil fuel methane emissions for the Global Fuel Exploitation Inventory (GFEI) v3, *Earth System Science Data Discussions*, 2025, 1–23, <https://doi.org/10.5194/essd-2024-552>, 2025.
- 735 Schaefer, H., Fletcher, S. E. M., Veidt, C., Lassey, K. R., Brailsford, G. W., Bromley, T. M., Dlugokencky, E. J., Michel, S. E., Miller, J. B., Levin, I., et al.: A 21st-century shift from fossil-fuel to biogenic methane emissions indicated by 13CH<sub>4</sub>, *Science*, 352, 80–84, [https://doi.org/DOI: 10.1126/science.aad2705](https://doi.org/DOI:10.1126/science.aad2705), 2016.
- Schneising, O.: Product User Guide (PUG) TROPOMI WFM-DOAS (TROPOMI/WFMD) XCH<sub>4</sub>, [https://admin.climate.esa.int/media/documents/PUG\\_CRDP9\\_v2\\_GHG-CCI\\_CH4\\_S5P\\_WFMD\\_v1.8.pdf](https://admin.climate.esa.int/media/documents/PUG_CRDP9_v2_GHG-CCI_CH4_S5P_WFMD_v1.8.pdf), 2024.

- 740 Schneising, O., Buchwitz, M., Reuter, M., Heymann, J., Bovensmann, H., and Burrows, J. P.: Long-term analysis of carbon dioxide and methane column-averaged mole fractions retrieved from SCIAMACHY, *Atmospheric Chemistry and Physics*, 11, 2863–2880, <https://doi.org/10.5194/acp-11-2863-2011>, 2011.
- Schneising, O., Buchwitz, M., Reuter, M., Bovensmann, H., Burrows, J. P., Borsdorff, T., Deutscher, N. M., Feist, D. G., Griffith, D. W., Hase, F., et al.: A scientific algorithm to simultaneously retrieve carbon monoxide and methane from TROPOMI onboard Sentinel-5 Precursor, *Atmospheric Measurement Techniques*, 12, 6771–6802, <https://doi.org/10.5194/amt-12-6771-2019>, 2019.
- 745 Schneising, O., Buchwitz, M., Reuter, M., Vanselow, S., Bovensmann, H., and Burrows, J. P.: Remote sensing of methane leakage from natural gas and petroleum systems revisited, *Atmospheric Chemistry and Physics*, 20, 9169–9182, <https://doi.org/10.5194/acp-20-9169-2020>, 2020.
- Schneising, O., Buchwitz, M., Hachmeister, J., Vanselow, S., Reuter, M., Buschmann, M., Bovensmann, H., and Burrows, J. P.: Advances in retrieving XCH<sub>4</sub> and XCO from Sentinel-5 Precursor: improvements in the scientific TROPOMI/WFMD algorithm, *Atmospheric Measurement Techniques*, 16, 669–694, <https://doi.org/10.5194/amt-16-669-2023>, 2023.
- 750 Sijkumar, S., Raju, A., Valsala, V., Tiwari, Y., Girach, I., Jain, C. D., and Ratnam, M. V.: High-Resolution Bayesian Inversion of Carbon Dioxide Flux Over Peninsular India, *Atmospheric Environment*, 308, 119 868, <https://doi.org/10.1016/j.atmosenv.2023.119868>, 2023.
- Skamarock, W. C., Klemp, J. B., Dudhia, J., Gill, D. O., Barker, D. M., Duda, M. G., Huang, X., Wang, W., and Powers, J. G.: A description of the advanced research WRF, National Center for Atmospheric Research, Boulder, CO), Version, 3, <https://doi.org/10.5065/D68S4MVH>, 2008.
- 755 Skeie, R. B., Hodnebrog, Ø., and Myhre, G.: Trends in atmospheric methane concentrations since 1990 were driven and modified by anthropogenic emissions, *Communications Earth & Environment*, 4, 317, <https://doi.org/10.1038/s43247-023-00969-1>, 2023.
- Solazzo, E., Crippa, M., Guizzardi, D., Muntean, M., Choulga, M., and Janssens-Maenhout, G.: Uncertainties in the Emissions Database for Global Atmospheric Research (EDGAR) emission inventory of greenhouse gases, *Atmospheric Chemistry and Physics*, 21, 5655–5683, <https://doi.org/10.5194/acp-21-5655-2021>, 2021.
- 760 Stevenson, D. S., Zhao, A., Naik, V., O’connor, F. M., Tilmes, S., Zeng, G., Murray, L. T., Collins, W. J., Griffiths, P. T., Shim, S., et al.: Trends in global tropospheric hydroxyl radical and methane lifetime since 1850 from AerChemMIP, *Atmospheric Chemistry and Physics*, 20, 12 905–12 920, <https://doi.org/10.5194/acp-20-12905-2020>, 2020.
- 765 Stocker, T. F., Qin, D., Plattner, G., Tignor, M., Allen, S., Boschung, J., Nauels, A., Xia, Y., Bex, V., Midgley, P., et al.: Contribution of working group I to the fifth assessment report of the intergovernmental panel on climate change, *Climate change*, 5, 1–1552, <https://doi.org/10.1017/CBO9781107415324.004>, 2013.
- Survey of India: Political map of India, <https://www.surveyofindia.gov.in/pages/political-map-of-india>, accessed on: 21 May 2024, 2024.
- 770 Thilakan, V., Pillai, D., Gerbig, C., Galkowski, M., Ravi, A., and Anna Mathew, T.: Towards monitoring CO<sub>2</sub> source-sink distribution over India via inverse modelling: Quantifying the fine-scale spatiotemporal variability of atmospheric CO<sub>2</sub> mole fraction, *Atmospheric Chemistry and Physics Discussions*, 2022, 1–38, <https://doi.org/10.5194/acp-22-15287-2022>, 2022.

- Thompson, R. L., Montzka, S. A., Vollmer, M. K., Arduini, J., Crotwell, M., Krummel, P. B., Lunder, C., Mühle, J., O'doherty, S., Prinn, R. G., et al.: Estimation of the atmospheric hydroxyl radical oxidative capacity using multiple hydrofluorocarbons (HFCs), *Atmospheric Chemistry and Physics*, 24, 1415–1427, 2024.
- 775 Turner, A., Jacob, D. J., Wecht, K. J., Maasackers, J. D., Lundgren, E., Andrews, A. E., Biraud, S. C., Boesch, H., Bowman, K. W., Deutscher, N. M., et al.: Estimating global and North American methane emissions with high spatial resolution using GOSAT satellite data, *Atmospheric Chemistry and Physics*, 15, 7049–7069, <https://doi.org/10.5194/acp-15-7049-2015>, 2015.
- Uma, K., Girach, I. A., Chandra, N., Patra, P. K., Kumar, N. K., and Nair, P. R.: CO<sub>2</sub> variability over a tropical coastal station in India: Synergy of observation and model, *Science of The Total Environment*, 957, 177 371, <https://doi.org/10.1016/j.scitotenv.2024.177371>,  
780 2024.
- Vellalassery, A., Pillai, D., Marshall, J., Gerbig, C., Buchwitz, M., Schneising, O., and Ravi, A.: Using TROPOspheric Monitoring Instrument (TROPOMI) measurements and Weather Research and Forecasting (WRF) CO modelling to understand the contribution of meteorology and emissions to an extreme air pollution event in India, *Atmospheric Chemistry and Physics*, 21, 5393–5414, <https://doi.org/10.5194/acp-21-5393-2021>, 2021.
- 785 Wang, Y., Yuan, Q., Li, T., Yang, Y., Zhou, S., and Zhang, L.: Seamless mapping of long-term (2010–2020) daily global XCO<sub>2</sub> and XCH<sub>4</sub> from the Greenhouse Gases Observing Satellite (GOSAT), Orbiting Carbon Observatory 2 (OCO-2), and CAMS global greenhouse gas reanalysis (CAMs-EGG4) with a spatiotemporally self-supervised fusion method, *Earth System Science Data*, 15, 3597–3622, <https://doi.org/10.5194/essd-15-3597-2023>, 2023.
- Wilcox, R.: *Trimming and Winsorization*, John Wiley Sons, Ltd, <https://doi.org/10.1002/0470011815.b2a15165>, 2005.
- 790 Yokota, T., Yoshida, Y., Eguchi, N., Ota, Y., Tanaka, T., Watanabe, H., and Maksyutov, S.: Global concentrations of CO<sub>2</sub> and CH<sub>4</sub> retrieved from GOSAT: First preliminary results, *Sola*, 5, 160–163, <https://doi.org/10.2151/sola.2009-041>, 2009.
- Zhang, X., Lee, X., Griffis, T. J., Baker, J. M., and Xiao, W.: Estimating regional greenhouse gas fluxes: an uncertainty analysis of planetary boundary layer techniques and bottom-up inventories, *Atmospheric chemistry and physics*, 14, 10 705–10 719, <https://doi.org/10.5194/acp-14-10705-2014>, 2014.
- 795 Zhang, Y., Jacob, D. J., Lu, X., Maasackers, J. D., Scarpelli, T. R., Sheng, J.-X., Shen, L., Qu, Z., Sulprizio, M. P., Chang, J., Bloom, A. A., Ma, S., Worden, J., Parker, R. J., and Boesch, H.: Attribution of the accelerating increase in atmospheric methane during 2010–2018 by inverse analysis of GOSAT observations, *Atmospheric Chemistry and Physics*, 21, 3643–3666, <https://doi.org/10.5194/acp-21-3643-2021>, 2021.
- Zhou, L., Warner, J., Nalli, N. R., Wei, Z., Oh, Y., Bruhwiler, L., Liu, X., Divakarla, M., Pryor, K., Kalluri, S., et al.: Spatiotemporal variability  
800 of global atmospheric methane observed from two decades of satellite hyperspectral infrared sounders, *Remote Sensing*, 15, 2992, 2023.